university of groningen

faculty of mathematics and natural sciences

Magnetoelasticity and Optically Induced Magnonic Crystals in CoFeB and Ni

THESIS

submitted in partial fulfillment of the requirements for the degree of

MASTER OF SCIENCE

in

APPLIED PHYSICS

Author :	R.R. Tamming
Student ID :	s2157233
Supervisor :	R.I. Tobey
2nd corrector :	T. Banerjee

Groningen, The Netherlands, July 21, 2017

Magnetoelasticity and Optically Induced Magnonic Crystals in CoFeB and Ni

R.R. Tamming

Zernike Institute for Advanced Materials, University of Groningen
P.O. Box 221, NL-9700 AE, Groningen, The Netherlands

July 21, 2017

Abstract

Multiferroics, materials that exhibit interactions between either magnetism, electricity and elasticity, show great potential in future applications. One of the multiferroic materials that has gained large interest is CoFeB due to the large resistance achieved in magnetic tunnel junctions at room temperature. The focus of this research is to obtain a better understanding of the spin dynamics by using the magnetoelastic interaction of CoFeB and compare it with the results previously found for Ni samples.

The experiments performed used an all-optical pump-probe setup, combined with a Faraday detection scheme to measure the change in polarization of the probe pulse. The setup is capable of introducing a second pump pulse, simultaneously with the first one, to create acoustic waves in the sample. Whilst doing this, an external magnetic field is applied, capable of rotating in-plane of the sample.

The results entails two parts of which the first is the determination of the magnetic anisotropic properties of CoFeB on SiO_x and MgO substrates by using the single pump-probe setup. Both of the samples exhibit uniaxial anisotropy which is more prominent in the MgO sample. The origin of the anisotropy remains unknown, however, magnetic fields are present during the fabrication which might induce magnetic ordering of the sample.

For the second part, the second pump is introduced. Via magnetoelastic interaction, spin precession is driven in both the CoFeB and the Ni sample at the resonant frequencies of the acoustic waves and the larmor precession. When rotating the magnetic field, the total signal shows unexpected behaviour. Whereas the magnetoelastic interaction predicts a $\sin(2\phi)$ relation for the precession signal, the obtained signal for CoFeB dissapears mostly after 30°. For Ni, there is a dip in the signal at 32°. The introduction of magnonic crystals and spin wave localization is made to explain this phenomenon, however, more research is required to get a full understanding.

Version of July 21, 2017– Created July 21, 2017 - 16:28

Acknowledgements

The first person I would like to thank is Ron Tobey for giving me a position as master student within the Optical Condensed Matter Physics group and introducing me to the world of optics and magnetoelasticity. I thank him for the guidance. He was always available for questions and discussions when times got tough. The second person I'd like to thank is Chia-Lin Chang, with whom I've collaborated closely during my stay at the group. He provided me with additional results necessary for my research and had vivid discussions about the subject. Julius Janušonis, thank you for clarifying the subject when I got confused. Next I would like to thank Darin Zwaan, who has done his master research simultaneously. We were always able to talk about the results either of us got, improving the understanding of the topic. For providing the logistic support I would like to thank Foppe de Haan for making sure the required software and hardware was available. Tamalika Banerjee, thank you for being my second supervisor and assessor. Furthermore, I'd like to thank Markus Münzenberg for providing the CoFeB samples. And I would like to thank Szymon Mieszczak and Jarosław Kłos for providing us with the numerical support.

Thanks to everybody from the Optical Condensed Matter Physics group for providing a nice and comfortable environment to work in. I enjoyed working (and taking breaks) with all of you.

Contents

1 Introduction **1**

2 Theory **4**

2.1 Acoustic Waves 4

2.2 Ferromagnetism 6

2.3 Ferromagnetic Resonance 7

2.4 Magnetic Anisotropy 9

2.5 Magnetoelastic Interaction 11

2.6 Magnonic Crystals 12

2.7 Faraday Effect 13

3 Experiment **15**

3.1 Sample Preparations 15

3.2 Pump-Probe Setup 16

3.3 Transient Grating Method 20

4 Results and Discussion **23**

4.1 Single Pump 23

4.2 Transient Grating 30

4.2.1 Acoustics on CoFeB 30

4.2.2 Acoustics on Ni 32

4.3 Spin Wave Localization 34

4.3.1 CoFeB 34

4.3.2 Ni 38

4.3.3 Ni wires 39

4.4 Discussion 41
4.4.1 Magnetic Anisotropy 41
4.4.2 Spin Wave Localization 43

5 Conclusion 45

Chapter 1

Introduction

In the era of information, data storage is a very important part of everyday life. The most common known example of a data storage device is the Hard Disk Drive (HDD), where small magnetic domains are set in particular directions to write the bits as shown in figure 1.1. Most of the data today is stored by using magnetism, creating a very active field of research to improve writing speed and reduce bit size, energy consumption and costs [1–4].

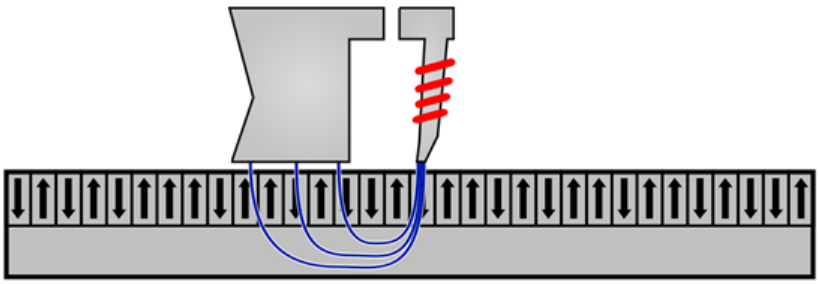

Figure 1.1: *Schematic overview of the working principle of a perpendicular writing head. Blue lines indicate the magnetic field created by the writing head.*

Multiferroic materials have gained interest in the past years due to their adaptable properties. Multiferroics are materials that show more

than one of the ferroic order parameters, which are Polarization, Magnetization and Strain, as shown in figure 1.2. These parameters are coupled and interact with each other via magnetoelectricity, ferroelasticity and magnetoelasticity. This behaviour enables the control of one of these ferroic order parameters by using the other, showing potential for a large range of applications.

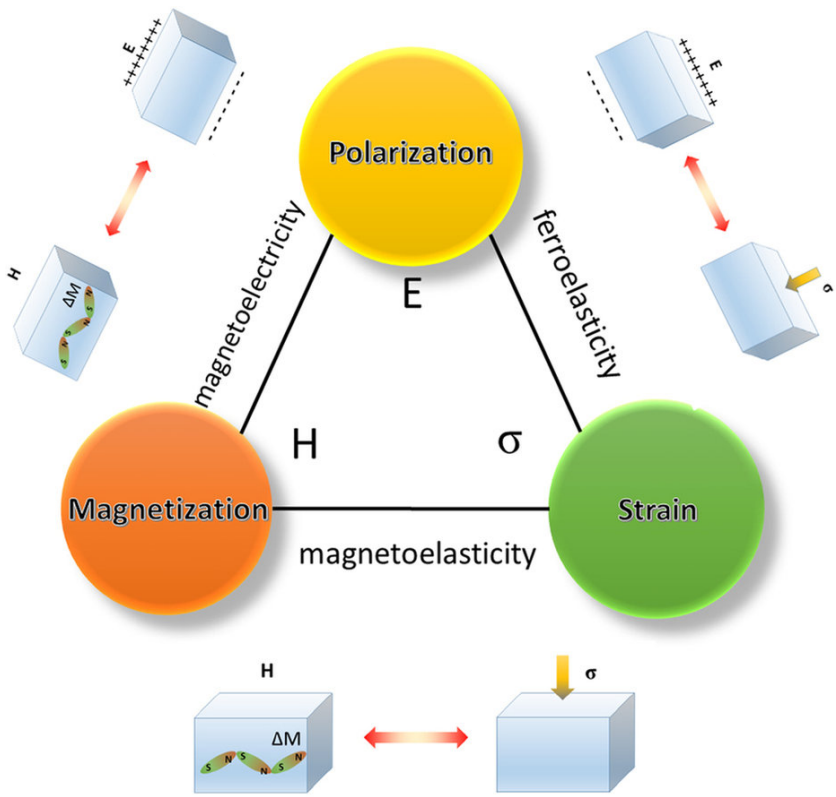

Figure 1.2: *The three ferroic order parameters and their interaction. Figure adapted from [5].*

The interaction exploited during this research is the magnetoelastic coupling in Cobalt Iron Boron (CoFeB) and Nickel. During this experiment, the interaction between the induced strain and the magnetization is observed. The method used to generate the strain which drives the magnetoelastic interaction is an all-optical method called Transient-Grating (TG)

spectroscopy. The data for the Ni sample is already available in the group since it has previously been investigated [6, 7].

CoFeB is an interesting material because it shows great potential for spintronic devices. Research has shown that it can be used in tunnel magnetoresistance (TMR) devices and a TMR of 604% at room temperature has been achieved [3, 8]. The purpose of this research is to compare the results of CoFeB sample with the Ni sample to obtain a better understanding of the spin wave manipulation.

Chapter 2

Theory

2.1 Acoustic Waves

The TG-setup used for this experiment is known to generate narrowband, frequency tunable high frequency surface waves. These high frequency waves are the so called acoustic waves. The two types of acoustic waves are generated; the Rayleigh surface acoustic wave (SAW) and the surface skimming longitudinal wave (SSLW).

The SAW is only present at the free surface of an elastic solid. One mode which is excited is the Rayleigh wave. It is represented by a time-dependent elliptical displacement of the surface structure, which means that there is a in-plane (y-direction) and out-of-plane (z-direction) motion of the sample surface as shown in figure 2.1. The equation of motion of the Rayleigh wave along the y-axis is given by

$$u = C \times e^{i(ky-\omega t)} e^{\kappa z} \tag{2.1}$$

where u is the displacement in either longitudinal or transverse direction, C is a constant determining the initial size of the displacement vector, k is the wave vector, ω is the wave frequency and κ is given by $\sqrt{k^2 - \omega^2/c^2}$. In this equation, c is the wave velocity, again in either longitudinal or transverse direction [9]. The true displacement **u** is given by the sum of the

longitudinal, u_l, and transverse displacement u_t with their corresponding c_l and c_t.

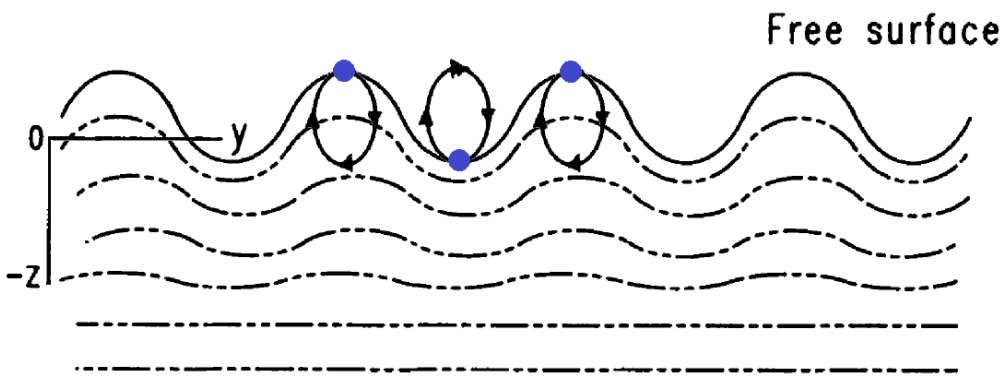

Figure 2.1: *Elliptical movement of the surface acoustic wave. Figure adapted and modified from [10].*

Since the depth the sample is given in the $-z$ direction, the displacement decreases exponentially with depth. Therefore the amplitude of the SAW motion, when looking looking at the depth of a few acoustic wavelengths, is quickly suppressed. The velocity of the acoustics will be mainly determined by the substrate because it's operated in the large wavelength limit ($\Lambda > 1\mu m$). Therefore the SAW velocity is $3120 \pm 20^{m}/_{s}$ for soda lime glass (SLG) with a grating of $1.1\mu m$ [6].

The second less known mode is the SSLW. This wave is some sort of longitudinal wave and not solely surface bound but has an in-plane component. This longitudinal wave is a weak shear wave which is transmitted into the bulk [11]. Therefore the amplitude of the SSLW is strongly attenuated over time and because of that, the wave is also known as the Leaky Surface Skimming Longitudinal Wave.

Whereas the SAW exhibits a strong surface deformation and surface bound behaviour, the SSLW is less surface bound. This statement is supported by Habib *et al.* [12] who have send a SSLW and a SAW through a $LiNbO_3$-crystal with a small piece of silver, but large compared to the

wavelength of either SAW and SSLW, on top of the crystal. The SAW is strongly attenuated and scattering is observed when passing along the silver particle. These phenomena are nearly absent for the SSLW showing that the propagation of the SSLW is mostly slightly below the surface.

When looking at the SSLW in SLG with a grating of $1.1\mu m$, the velocity is about $5590 \pm 15^{m}/_{s}$ which is almost twice as large compared to the SAW velocity of $3120 \pm 20^{m}/_{s}$ stated earlier. The change in velocity, and thus frequency, can be used to quickly identify the two characteristic waves.

2.2 Ferromagnetism

The magnetoelastic interaction in a multiferroic has an elastic part, as discussed in the previous section, and a magnetic part. When looking closely at the magnetic properties of the ferromagnet, this is governed by spins. One of the properties of a ferromagnet is its spontaneous magnetic moment in absence of an external magnetic field [13, 14].

When applying an external field, the magnetization M is given by

$$\mu_0 M = \chi_p (H + B) \tag{2.2}$$

where χ_p is the paramagnetic susceptibility, which is positive for a ferromagnet and negative for an antiferromagnet. H is the applied field and B is the exchange field of the ferromagnet. The exchange field is the interaction one spin has to its neighboring spins which is the cause of the alignment of the spins to reach the lowest possible energy state within a ferromagnet.

When increasing the temperature, the spin order will decrease until it is completely destroyed. The temperature at which the order is completely absent is called the Curie temperature. From experimental data, the magnetization is given by the Bloch $T^{3/2}$ Law:

$$\frac{\Delta M}{M_0} = AT^{3/2} \tag{2.3}$$

where ΔM is the change in magnetization, M_0 the magnetization at zero temperature, T is the temperature and A is an empirical constant, depending on the material. For Ni, the latter value is determined to be $(3.4 \pm 0.2) \cdot 10^{-6}\mathrm{K}^{-3/2}$. This equation is later solved via the quantization of spin waves and is given to be

$$\frac{\Delta M}{M_0} = \frac{0.0587}{SQ} \left(\frac{k_B T}{2JS} \right)^{3/2} \tag{2.4}$$

where S is the spin state, Q is the atomic packing factor and J is the exchange integral [13, 14].

2.3 Ferromagnetic Resonance

The first experimental data on ferromagnetic resonance (FMR) is recorded by Griffiths [15]. This was done by putting a thin film of Ni at one end of a cylindrical resonator. A static magnetic field is applied in the plane of this film. A microwave generator is used to generate a microwave field in a constant direction, where the magnetic component is perpendicular to the applied field direction. When measuring the energy loss in the cavity, a maximum in loss is occurring at the FMR frequency due to the energy being absorbed by the Ni film.

Griffiths stated that the energy loss in the cavity was due to the resonant absorption by the magnetic dipoles. However, no concluding theory was formulated. After a short while a theory was proposed on the resonance effect by Kittel [16]. FMR is the uniform precessional motion of the magnetization of a ferromagnet in an externally applied field. The external field causes a torque on the magnetic dipole, inducing the precessional motion.

The differential equation describing the dynamic magnetization motion in a solid is called the Landau-Lifshitz-Gilbert (LLG) equation and is

given by

$$\frac{\partial \mathbf{M}}{\partial t} = -\gamma \mathbf{M} \times \mu_0 \mathbf{H} + \alpha \mathbf{M} \times (\mathbf{M} \times \mathbf{H}) \tag{2.5}$$

where γ is the gyromagnetic ratio of the used sample and α is the Gilbert damping constant [17]. The Gilbert damping constant is the rate at which the magnetic moment relaxes to its equilibrium. The representation of this precessional motion is given in figure 2.2

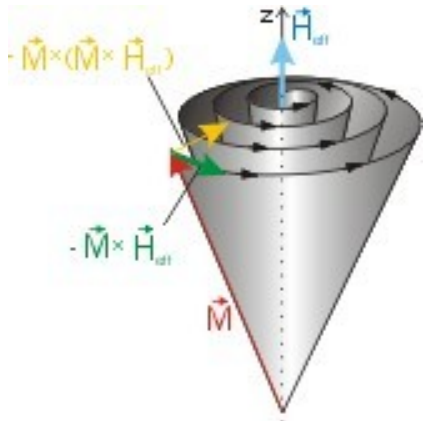

Figure 2.2: *Schematic of the FMR precession of a single spin*

By solving the LLG equation, it is possible to derive the frequency of the precession. The FMR frequency is given by the famous Kittel equation:

$$\omega = \gamma \sqrt{H(H + \mu_0 M_s)} \tag{2.6}$$

where H is the strength of the external applied field and M_s is the saturation magnetization [13]. The curve given by the Kittel equation is not a narrow solution, but shows a Lorentzian distribution depending on the applied field. The linewidth of the FMR is dependent on the sum of the inhomogeneous part and a part due to the Gilbert damping of the material and is given by

$$\Delta H = \Delta H_0 + \frac{2\alpha}{\mu_0 \gamma} \omega \tag{2.7}$$

where ΔH_0 is the inhomogeneous broadening which describes spatial variations in the saturation magnetization M_s or anisotropy conditions which

have a small variation within the material [18]. When integrating over the different conditions within the material, this results in a frequency independent broadening. The second term is frequency dependent and is the result of the Gilbert damping [19]. This term increases for higher frequencies and by using the Kittel equation, broadens the FMR for higher field strengths because of the increase in precessional frequency.

2.4 Magnetic Anisotropy

Magnetic anisotropy is the directional dependence on the material's magnetic properties. During this section, uniaxial anisotropy is discussed. Uniaxial anisotropy means there is one easy axis and one hard axis. Due to the energy landscape, the net magnetization of the material tend to align with the easy axis since this is the state of lowest energy. An example of the uniaxial magnetic energy landscape is given as figure 2.3. Because the

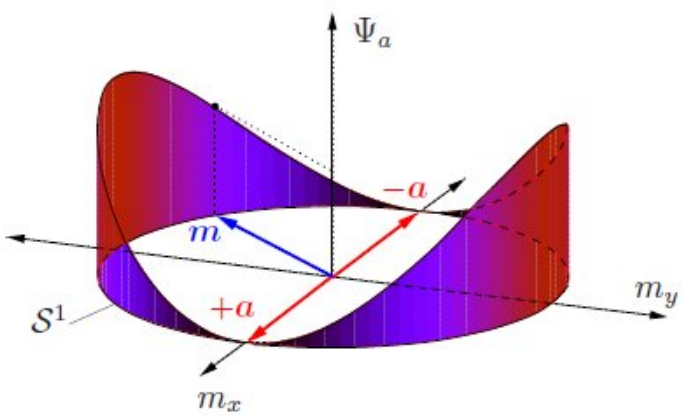

Figure 2.3: *Directional energy dependence for magnetization in a 2D case. Here the easy axis is in the $(-)x$ direction and the hard axis is given in the $(-)y$ direction. As seen is the direction of the magnetization (blue arrow) not in it's favorable position, but rather at a higher energy state.*

energy is lowest at the easy axis, the magnetization will lie along that direction without external field. When applying an external magnetic field,

the minimum directional energy will shift towards the external field, misaligning from the easy axis. The result is a magnetization between the easy axis and the applied field. The final magnetization direction is dependent on the applied field strength and anisotropy constant. The magnetization will only align with the external field when a sufficient high field is applied.

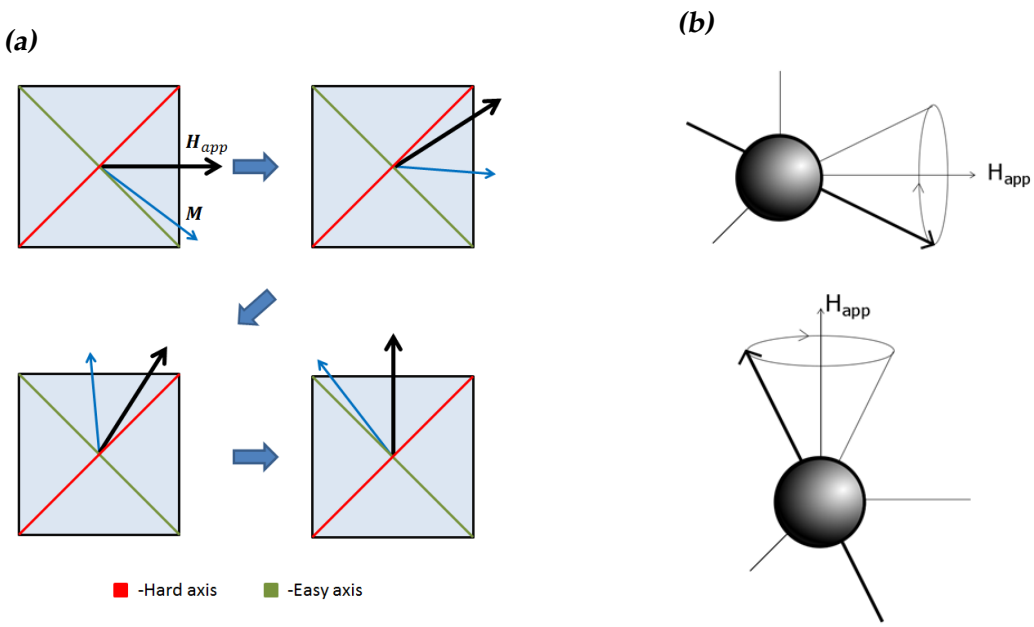

Figure 2.4: *(a) Illustration of the angle of effective magnetization, M, of the sample for different angles of applied field, H_{app}. (b) Precession direction of the spin on different applied field angles relative to the net magnetization direction.*

Figure 2.4a gives a representation of the effect of the uniaxial anisotropy on the magnetization direction for different applied field angles. As seen from this image, the effective magnetization flips to the other side of the external field when the external field passes the hard axis. This initiates the starting direction of the rotation to be in opposite direction as shown in figure 2.4b. When coming closer to the easy axis, the frequency change will decrease and the signal will disappear when aligned with the easy axis since no torque is applied on the spins.

In-plane uniaxial magnetic anisotropy in amorphous CoFeB has been reported under specific growing or magnetostrictive conditions [20, 21]. Besides these conditions, CoFeB is capable of having in-plane uniaxial anisotropy when mixed with SiO_2 as shown by Manuilov *et al.* [22]. Thin film CoFeB is better known for its out-of-plane magnetocrystalline anisotropy and has been used extensively for GMR and other spintronic devices [23–25].

2.5 Magnetoelastic Interaction

So far the acoustics and the relevant ferromagnetic properties are explained. However, the two of them are coupled in the world of multiferroics. The coupling between the acoustics and the magnetism is via magnetostriction. Magnetoelasticity is treated in the framework of free energy to obtain understanding of the interaction.

The free energy for the magnetoelastics is given by

$$F(t) = b_1[\epsilon_{xx}M_x^2 + \epsilon_{yy}M_y^2 + \epsilon_{zz}M_z^2] + b[\epsilon_{xy}M_xM_y + \epsilon_{xz}M_xM_z + \epsilon_{yz}M_yM_z] \tag{2.8}$$

where b_1 and b are magnetoelastic coefficients, ϵ is the strain tensor and M_x, M_y and M_z are the magnetization components [26].

Because of this time-dependent contribution to the free energy of the system, the LLG equation 2.5 does not have a static magnetic field, but it becomes time dependent. The magnetic field is now given by

$$\mathbf{H}(t) = \frac{1}{\mu_0}\frac{dF(t)}{d\mathbf{M}} \tag{2.9}$$

By differentiating the free energy with respect to the magnetization and filling it in equation 2.5 results in the change of magnetization is described by

$$\frac{d\mathbf{M}}{dt} = \hat{x}(2b\epsilon_{xz}M^2\sin\phi\cos\phi) + \hat{y}(-2b\epsilon_{xz}M^2\cos^2\phi) + \hat{z}(2b\epsilon_{xx}M^2\sin\phi\cos\phi) \tag{2.10}$$

where ϕ is the direction of the applied field. No strain in the y-direction is assumed to simplify the system. This assumption can be made since the strain generated is only in the x and z-direction in the used setup as will be discussed in section 3.3.

The method used to measure the magnetic response is based on the Faraday effect which will be explained in section 2.7. Important for now is to know that the measured magnetization is the magnetization in the out of plane direction, which is the z-direction. Therefore the equation simplifies to

$$\frac{d\mathbf{M}}{dt} = \hat{z}[b\epsilon_{xx}M^2 \sin(2\phi)] \tag{2.11}$$

which is dependent on the strain in the x-direction and the angle of the applied magnetic field. This means that the compression and expansion have opposite sign of change in magnetization. Another feature is a zero change in magnetization over time in the z-direction when applying an external magnetic field at $0°$, $90°$, $180°$ $270°$.

2.6 Magnonic Crystals

A magnonic crystal (MC) is created when a ferromagnet is spatially modulated to change its structural or magnetic properties [27]. These crystals are periodically modulated and may have a layered (1D), striped (2D) or dotted (3D) pattern as shown in figure 2.5. The band structure of the ferromagnetic MC does not only depend on the periodic patterning, but is also governed by the spatial arrangement of the magnetization. The latter can easily be influenced which enables the control over the wave properties in these crystals.

Within a ferromagnetic MC, spin waves show dispersion relations which are dependent of the applied wavevector, the strength and orientation of the external magnetic field, the shape of the magnet and the magnetocrystalline anisotropy. This provides precise control over the interesting properties of the spin waves such as frequency, phase, velocity and amplitude.

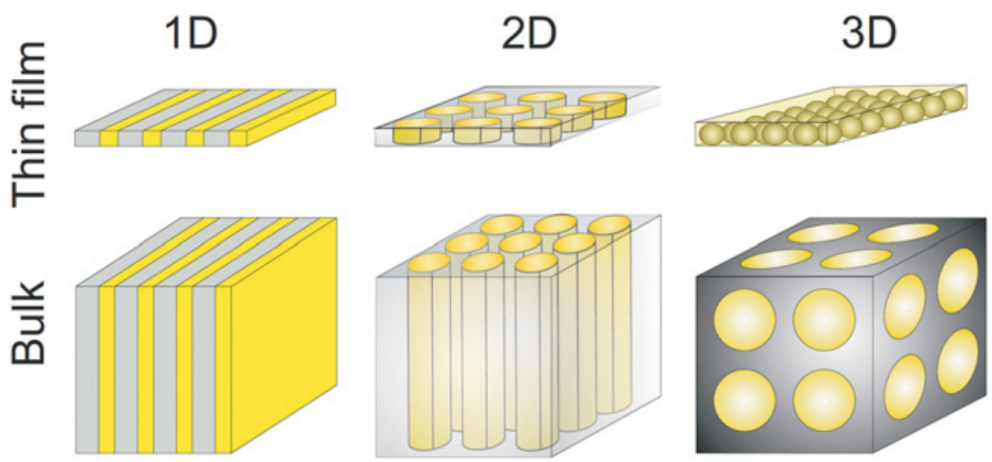

Figure 2.5: *The different dimension possible for a magnonic crystal. Figure adapted from [28].*

2.7 Faraday Effect

The faraday effect was first described and measured by, as the name suggests, Faraday [29]. He discovered that the polarization of a ray of light rotates when passing through a medium under the influence of a magnetic field. A slightly adapted overview of the experiment Faraday conducted is given in figure 2.6. The magnets Faraday used were two strong horseshoe shaped magnets instead of the coil as presented in the figure, but the phenomenon remains the same.

The rotation angle of the polarization β is empirically determined to be

$$\beta = \mathscr{V} B d \tag{2.12}$$

where B is the magnetic flux density out-of-plane of the sample and d the distance of light travelled through the medium [30]. At last, $\mathscr{V}$ is the Verdet constant. This constant is dependent on the medium, frequency and temperature and can either be positive and negative as shown in Jain *et al.* [31] by increasing the concentration of ferric ions in the water, which is used as medium.

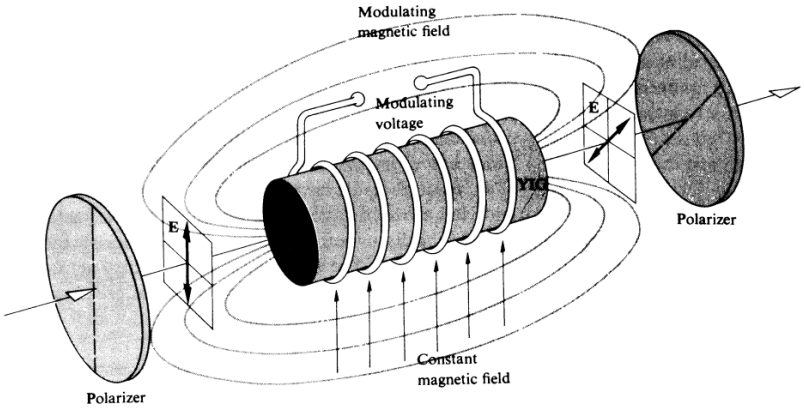

Figure 2.6: *The experiment Faraday has conducted to be able to measure the interaction of a magnetic field on light when passing through a medium. The left polarizer ensures polarized light entering the medium and the angle at which the light is rotated is measured with the second polarizer. Figure adapted from [30].*

As stated, B is the magnetic flux density of the out-of-plane component meaning that only the out-of-plane magnetic component can be measured using this method. The direction of the magnetization during the spin precession will have a time-dependent component in the z-direction. Because of this, the outgoing beam will obtain a time-dependent polarization direction, carrying the information on the magnetic state of the sample. By using a Wollaston prism, the s and p-type of polarization can be spatially separated and the intensity can be measured independently. The difference in signal between the two photodetectors is used to calculate the spin precession frequency.

Chapter 3

Experiment

3.1 Sample Preparations

For the experiment, comparisons are made between CoFeB and Ni. The CoFeB samples used are obtained from the Grenz- und Oberflächenphysik group in Greifswald. There are two different types of substrates used during this experiment. The first substrate is Silicon Oxide (SiO_x), and the second substrate is magnesium oxide (MgO). On top of these substrates, a $40nm$ layer of amorphous $Co_{20}Fe_{60}B_{20}$ is deposited using DC sputtering and is capped by $2nm$ of ruthenium. The capping layer is to prevent the sample from oxidizing and is thin enough to prevent contributions to the signal.

The Ni sample is made by using e-beam evaporation. A layer of $40nm$ is deposited on a SLG substrate with no further capping layer. This is not required since previous results have shown no deterioration of the sample over time.

The intrinsic Gilbert damping constant for the CoFeB is determined to be 0.004 [32]. Iihama *et al.* [33] show the same result for the CoFeB sample and also show that the MgO substrate has near to no influence on the Gilbert damping for a thickness of $40nm$. The same holds for the ruthenium capping layer as shown by Natarajarathinam *et al.* [34] and

therefore the damping constant is assumed to be purely intrinsic.

The damping constant for Ni is determined by Walowski *et al.* [35] to be 0.0453, which is a factor of 10 higher. Therefore the precession of CoFeB is expected to persist for a longer time compared to the precession of Ni. Another result on which the Gilbert damping has influence is the width of the ferromagnetic resonance as can be seen from equation 2.7. For CoFeB, the Gilbert damping is much lower compared to Ni, resulting in a smaller broadening from the second term.

The saturation magnetization M_s for CoFeB is about $1.7T$ [24, 32], depending on its exact composition. The saturation magnetization is the minimum value of the external applied field at which the internal field of a ferromagnet is as aligned as the crystal structure allows.

Ni has a saturation magnetization of $0.66T$ [35], which is only one third of that of CoFeB. The expected change in signal resulting from this property can be obtained from the Kittel equation given by 2.6. When increasing the saturation magnetization in this equation, the slope of the FMR frequency increases. Therefore lower fields are necessary to achieve the magnetoelastic resonance conditions between the FMR and the acoustic waves.

3.2 Pump-Probe Setup

For this experiment, a Titanium Sapphire (Ti:Sapphire) oscillator is used. This crystal is known for its large emission spectrum which lies between about $650nm$ and $1100nm$, while for this setup the wavelengths between $700nm$ and $900nm$ are selected by the mirror properties. The amplifier emits pulses with a FWHM of $120fs$ which are send through an amplifier. This amplifier increases the power of the pulses and generates a pulse repetition rate of $1kHz$.

After the amplifying system, the beam is split in a pump and probe beam as shown in figure 3.1. The pump beam is directed through a vari-

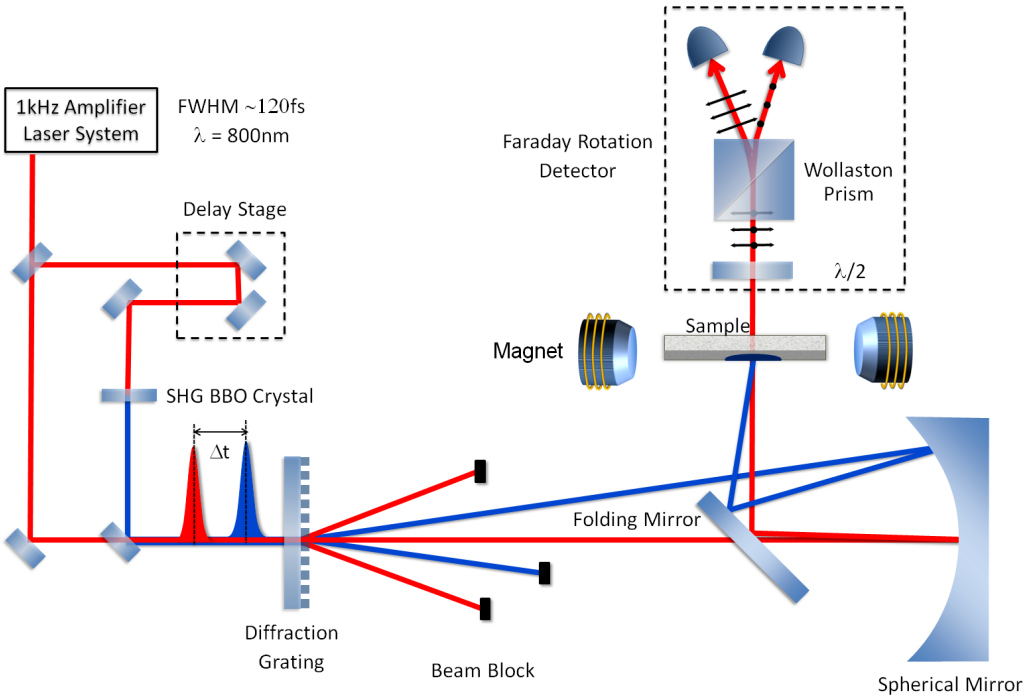

Figure 3.1: *Schematic overview of a single pump-probe system.*

able delay stage while the probe is directed through a fixed delay to be able to match time zero, at which both the pump and probe arrive at the same time. After the delay stage, the pump is chopped at $500Hz$ to synchronize with the frequency of the lock-in amplifier and is send through a doubling crystal to decrease the wavelength to $400nm$. The probe beam is kept at the fundamental wavelength centered around $800nm$, obtained from the Ti:Sapphire laser. The choice of wavelength is somewhat arbitrarily, but is appropriate since enough of the pump beam is absorbed and enough of the probe beam is transmitted to measure a signal. The doubling crystal is set in place to be able to differentiate in the colors, which allows the use of color filters to only select the probe beam to enter the detectors thereby increasing signal-to-noise ratio. Also, the decreased wavelengths enables a higher resolution grating (if required). The total range of the delay stage is about $8ns$ after time zero, providing a sufficient range to observe the dynamic response.

The beams are directed through a diffraction grating, where all diffraction beams but one of the first order of the pump and the zeroth order of the probe are blocked. This part is not required for this setup, but it makes it easier to switch to the transient grating technique discussed in the next section. After the grating, the beams recombine at the sample surface with a variable time delay to measure the magnetic response in time of the material after the pump. The delay stage is set at a certain position for a short while to be able to integrate over multiple measurements. This means that for a certain time delay, multiple probe signals are detected.

During this experiment, an electromagnet is placed in-plane of the sample surface which is able to rotate around the sample in the in-plane configuration between -45 and 230 degree relative to the horizontal axis, giving the possibility to do in-plane angle dependent applied field measurements whereas other research groups mostly have fixed angles [36, 37] or perform out-of-plane measurements [38].

An increase in temperature will occur when hitting the sample by the pump beam. The temperature comes closer to the Curie temperature, decreasing the magnetization of the sample [39]. Thereby the equilibrium position is tilted which starts the FMR precession. When the heat is diffused, the equilibrium position has restored to its pre-time zero configuration, but since the initial precession the precession will continue to persist.

Upon transmission through the sample, the Faraday effect will alter the polarization of the light as explained in section 2.7. This is possible because the spin precession driven by the pump beam has an out-of-plane component. After the probe has been transmitted through the sample, the Wollaston prism is used to split the beam by polarization in order to measure the magneto-optical dynamics. The index of refraction is dependent on the polarization, which enables this prism to spatially separate the two polarizations and measure their intensity separately on two detectors. The signal of the one of the detectors is subtracted from the other to obtain the difference in signal and thereby the magnetic response of the sample after

excitation, dependent on applied magnetic field angle and field strength can be observed.

The signal coming on the two detectors before time zero is balanced by using a $\lambda/2$ wave plate, which means that the intensity on both detectors are the same which result in zero signal. Since the sample used during the experiment is magnetized in plane, no change in signal appears when turning the magnet on as can be seen from equation 2.12, which states that an out-of-plane magnetic field within the magnetic material is required.

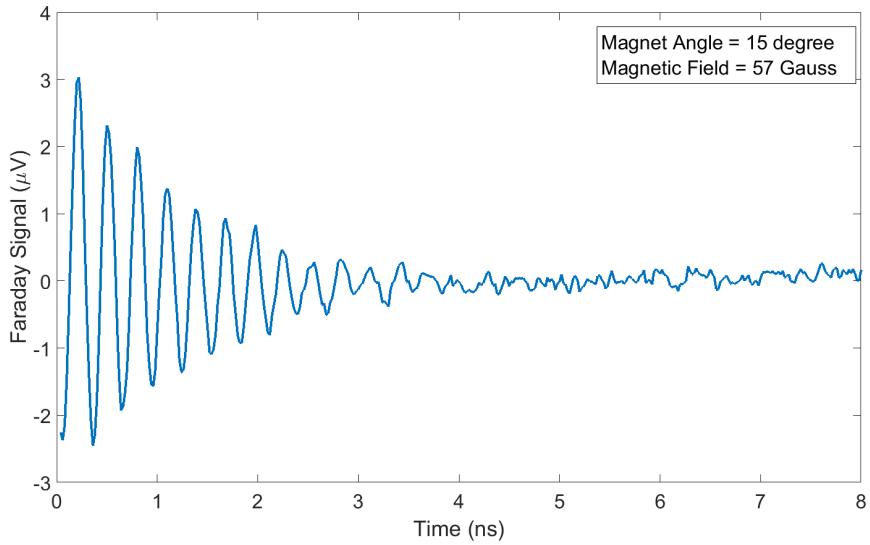

Figure 3.2: *Single timetrace for a single pump experiment on CoFeB/MgO showing the FMR using the Faraday signal.*

Figure 3.2 shows the typical time trace of a single pump-probe measurement of CoFeB/MgO, where the Faraday signal on the detectors over time is shown. The details of this plot will be discussed later in this report. The frequency of the precession is determined by taking the fast fourier transform (FFT) by using the build-in Matlab function.

This figure shows the response at a specific magnetic field condition. The setup is capable of adjusting the angle of the magnet and the field strength. By fixing one of the parameters and varying the other, multi-

ple of these scans can be made. These scans are shown in contour plots, having the varying parameter on the x-axis and time or frequency on the y-axis. The amplitude of the signal is represented by the colorscheme.

3.3 Transient Grating Method

To measure the magnetoelastic response of the samples, a setup based on the work of Janušonis *et al.* [7] is used. This setup enables non-contact excitation and detection of the surface magneto-elastic waves at (very) short timescales. This TG technique is applied on the material to generate acoustic waves in the material. These acoustic waves are the SAW and SSLW waves as discussed in section 2.1.

To obtain the TG setup, a small change of the setup previously discussed is required. The adapted setup is displayed in figure 3.3. By removing the block of the second first order pump beam after the grating and using a spherical mirror to recombine the two beams, an interference pattern is projected on the sample surface.

Figure 3.4 shows a schematic of the interference pattern created by the transient grating method, inducing hot (red) and leaving cold (blue) regions on the sample surface. The hot regions cause expansion of the sample and its substrate while the cold region is being compressed. This compression and expansion of the sample launches the SAW and the SSLW at the frequency of the substrate [40, 41].

The definition of the grating period, Λ, is indicated in this figure. Keep in mind that this figure is just a schematic overview. The probe beam has a diameter of $400\mu m$ and the probe has a diameter of $80\mu m$. Therefore in reality, there are approximately 70 interference lines within the area of the probe beam and the Faraday signal measured by this setup is the integral over the total area of the probe beam. Therefore it measures the average state of the excited sample.

The applied diffraction grating, having a certain grating constant, de-

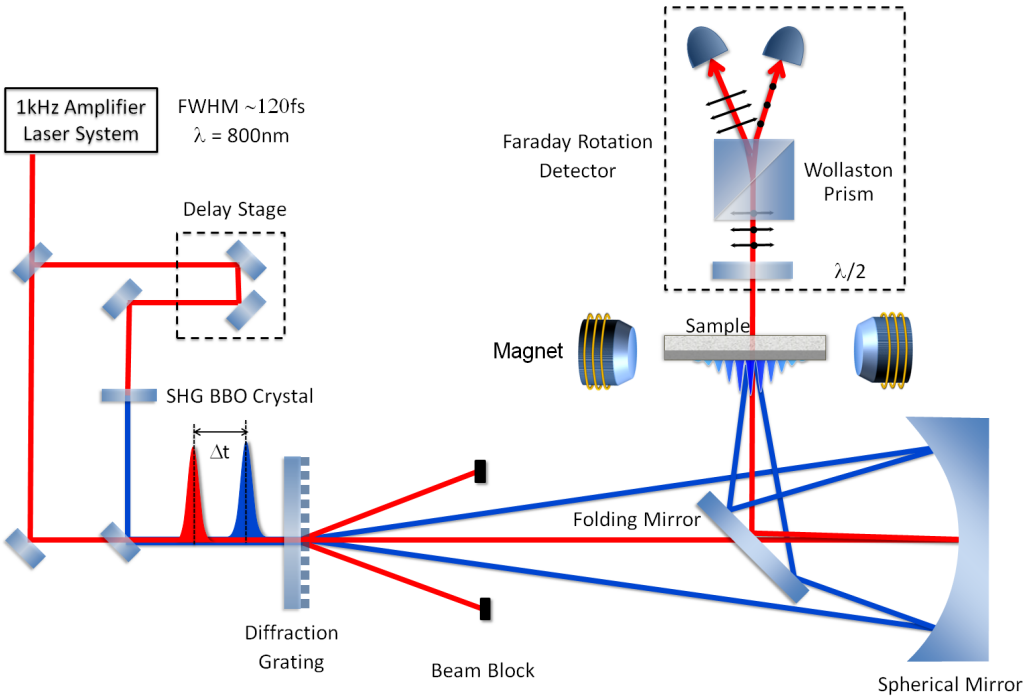

Figure 3.3: *Schematic overview of the transient grating setup. The setup is the same as the one used for single pump-probe with the exception of the removal of the beam block for the second first order pump beam.*

termines the angle between the two first order diffraction lines according to

$$a \sin \theta_m = m\lambda \tag{3.1}$$

where a is the distance between the slits in the grating, θ_m is the angle of the mth order maxima and λ is the wavelength of the light [30].

Upon recombining the two beams by using the spherical and folding mirror, the angle between the two pumps is dependent on the applied grating. The grating wavelength is dependent on this angle and the relation is given by

$$\Lambda = \frac{\lambda}{2\sin(\theta/2)} \tag{3.2}$$

where Λ is the grating wavelength, λ is the wavelength of the light and θ is the angle between the two pump pulses [40]. Therefore, the angle of

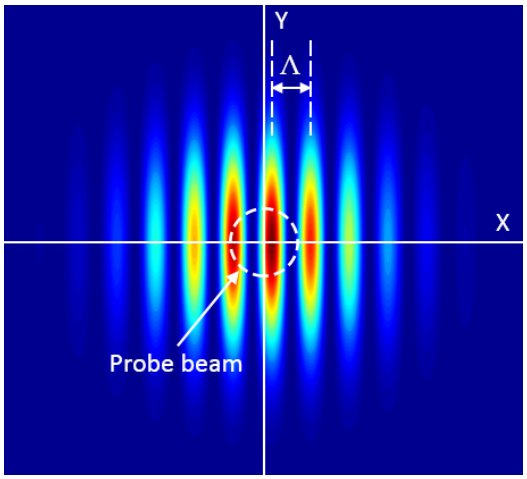

Figure 3.4: *Interference pattern projected on the sample surface. The red colour show the hot regions while the blue part is the cold region. Λ is the grating period which can be adapted according to equation 3.2.*

recombination is dependent on the grating period which is applied and can easily be adapted to experiment with different grating wavelengths. During the course of the experiment one grating period Λ of $1.1\mu m$ is used.

In addition to generating the acoustic waves, another response should be considered. The creation of a magnonic crystal, induced by the temperature profile. When looking at figure 3.4 again, a periodic modulated temperature profile can be observed along the x-axis. This induces a periodic modulated magnetization, a MC, where there is a low magnetization at the high temperature regions and a high magnetization at the low temperature regions. This optically induced MC has a life span of a couple of nanoseconds in which the temperature redistributes over the sample, resulting in a uniform decrease in saturation magnetization.

Chapter 4

Results and Discussion

The measurements will be shown and explained during this chapter. First, only the magnetic response on a single pump-probe on CoFeB and its anisotropy will be discussed. Secondly, the second pump is introduced and thereby creating acoustic waves in the CoFeB and Ni samples which, via inverse magnetostriction, are capable of driving spin precession.

4.1 Single Pump

During the initial measurements of CoFeB/MgO, unexpected results were obtained. By using the single pump-probe setup and an in-plane magnetic field, an oscillating signal was observed without the generation of the acoustic waves. Since this response is not present at the Ni measurements, the origin of the signal has to come from the sample properties rather than the used setup. For the Ni sample the magnetization was in the same direction as the applied field, except when the applied field was tilted out-of-plane because of it's . Therefore, the measured oscillation was the first indication of magnetocrystalline anisotropy. To investigate this phenomenon, field scans are taken over the magnet angle and magnetic field strength.

Figure 4.1 shows the contour plot for the time traces for the angle de-

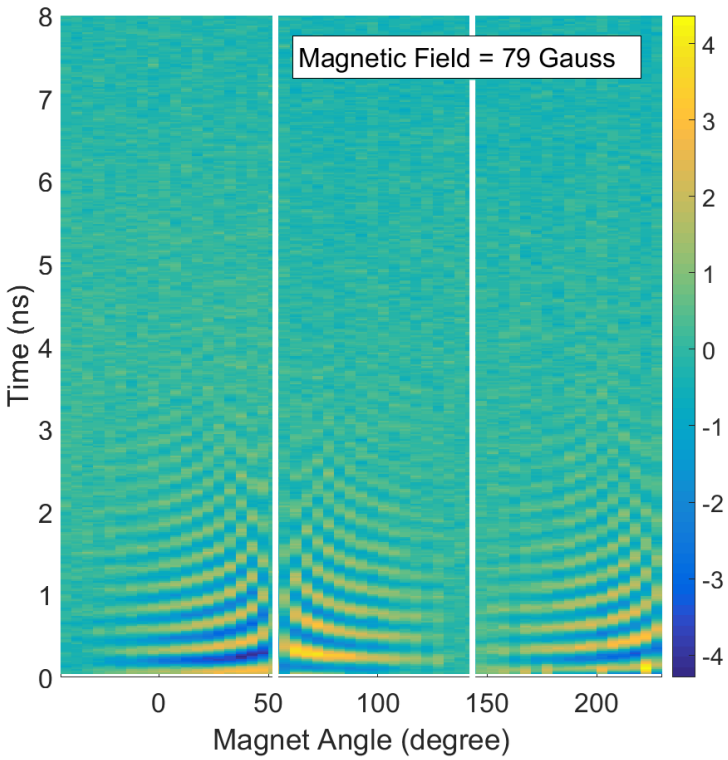

Figure 4.1: *Time traces for CoFeB/MgO for changing applied magnetic field angle. The scale on the right is the obtained difference in signal from the two detectors and is given in μV.*

pendent measurement on CoFeB/MgO for the single pump measurement. One vertical line is one time-trace at a particular magnet angle. The signal level tells about the difference in signal obtained by the two detectors which measure the intensity of the polarization.

The first thing that should be noticed is the change of sign of the signal around approximately 53° and 143°. So when looking at $(53° - \Delta\phi_H)$ and $(53° + \Delta\phi_H)$ the response has opposite phase. This is more clearly shown in figure 4.2 where the single time traces for 50° and 55° are shown, which are both about equally distanced from the position at which the phase changes.

The reason for this change of phase is because of the change in the po-

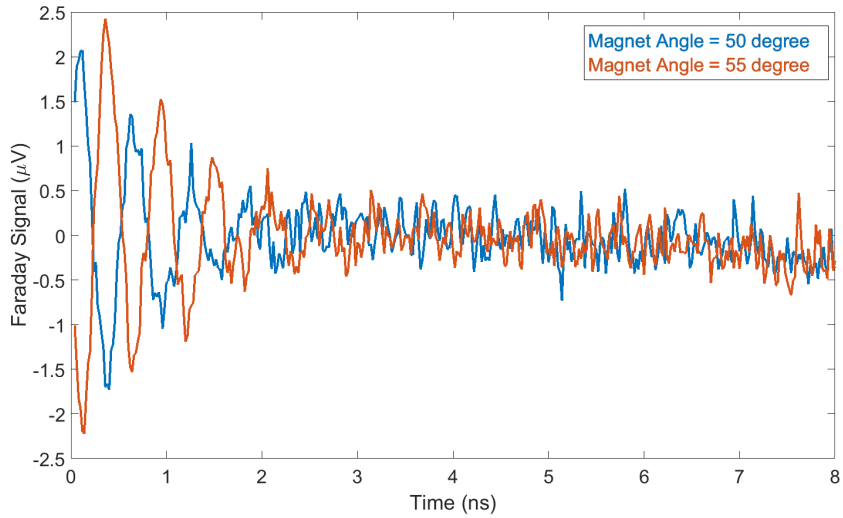

Figure 4.2: *Time traces for CoFeB/MgO for particular angles around the hard anisotropy axis. A field of 79 Gauss is applied.*

sition of the magnetization relative to the applied field direction, which changes the initial direction of the precession at time zero. As discussed in section 2.4, the relative position will change when crossing either the hard or easy axis, resulting in the change of initial direction of the precession. This initial change of direction causes a 180 degree phase shift. This suggests there is some sort of anisotropy in the system. Since a second type of crossing can be pointed out at about 143°, the system is likely to have an uniaxial anisotropy since the angle between the hard and easy axis are 90°. So is the left part of figure 4.1 between about −40° and 53° is similar to the right part between 143° and 230°.

The hard and easy axis can be identified by using this figure. Around 143° and −40° the change of frequency is very small. The change in frequency is better seen in the Fourier transform of the time trace given in figure 4.3. This small change can be explained by the free energy of the system which needs to be minimized. Since magnetic alignment with the easy axis has a low energy state, the magnetization tends to align with this axis when no external field is applied. When an in-plane external

field is applied, the magnetization will be slightly tilted from the easy axis towards the applied field. The magnetization will therefore always lie between the easy axis and the applied field and a certain deviation in applied field angle near the easy axis will result in a smaller deviation of the magnetization direction.

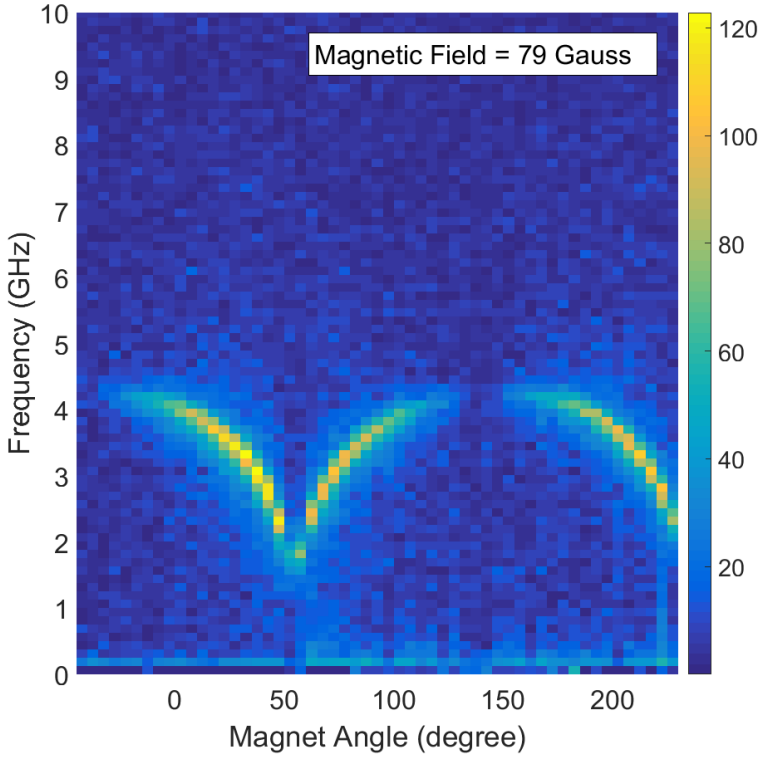

Figure 4.3: *Fourier transform of the time-traces of figure 4.1 on CoFeB/MgO.*

Since the hard axis required a lot of energy for the magnetic field to align in, it will only be fully aligned in this direction if the external magnetic field is aligned. A small deviation close to the hard axis will result in a large change of the magnetization angle since the magnetization has to cross the applied field angle. Because the magnetization is still between the easy axis and the applied axis, the angle will quickly change from one side to another when crossing the hard axis having large frequency deviation around this angle. This large change of frequency happens at the

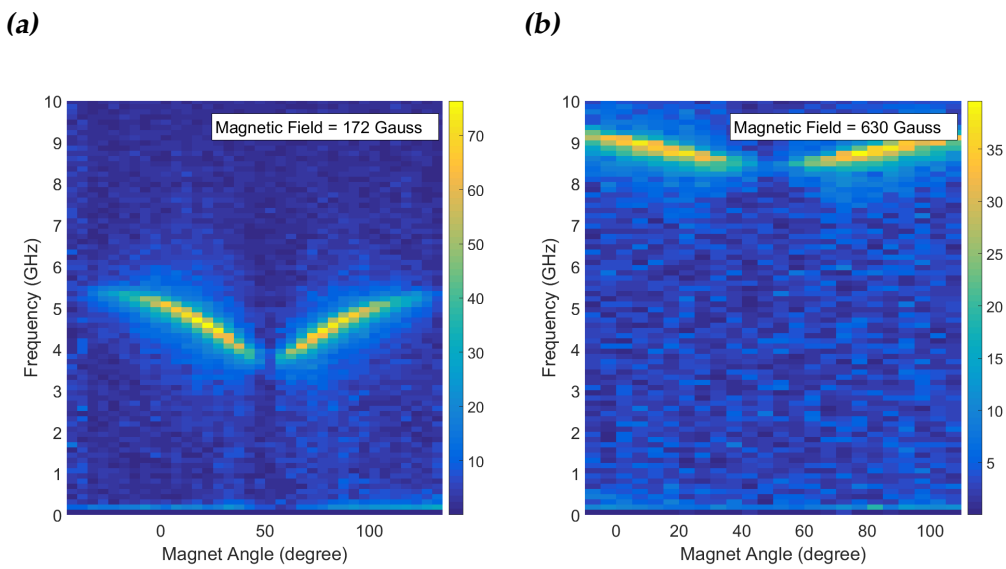

Figure 4.4: *Angular dependence resonance frequency for CoFeB/MgO for the single pump-probe experiment for two field strengths.*

vicinity of 53° and 230°, identifying these angles as hard axis.

According to the Kittel equation 2.6 the frequency of the FMR increases with increasing applied field. When looking at figures 4.3 and 4.4 it can be concluded that when the field increases, so does the frequency. Note here that the angle at which the hard and easy axis are stay the same and are independent of field strength.

When using a fixed magnetic field angle but varying the field strength, figure 4.5 is obtained at an applied field angle of 15 degree. From figure 4.5b can be seen that the FMR frequency increases for increasing field strength. This is expected from the Kittel equation. When comparing the frequency for the known applied field strengths as discussed earlier, the results match nicely.

The frequency for $79Gs$, $172Gs$ and $630Gs$ are $3.6GHz$, $5.0GHz$ and $9.3GHz$ respectively at an angle of $15^{c}irc$. For the field dependent scan, the frequency at an applied magnetic angle of 15° are $3.8GHz$, $4.9GHz$ and $9GHz$. There is some room for error here since the sample has been

taken out and put back in place, changing the angle of the anisotropy angle slightly. Another possibility is the error in the magnet position, but this should be limited by $\pm 0.5°$.

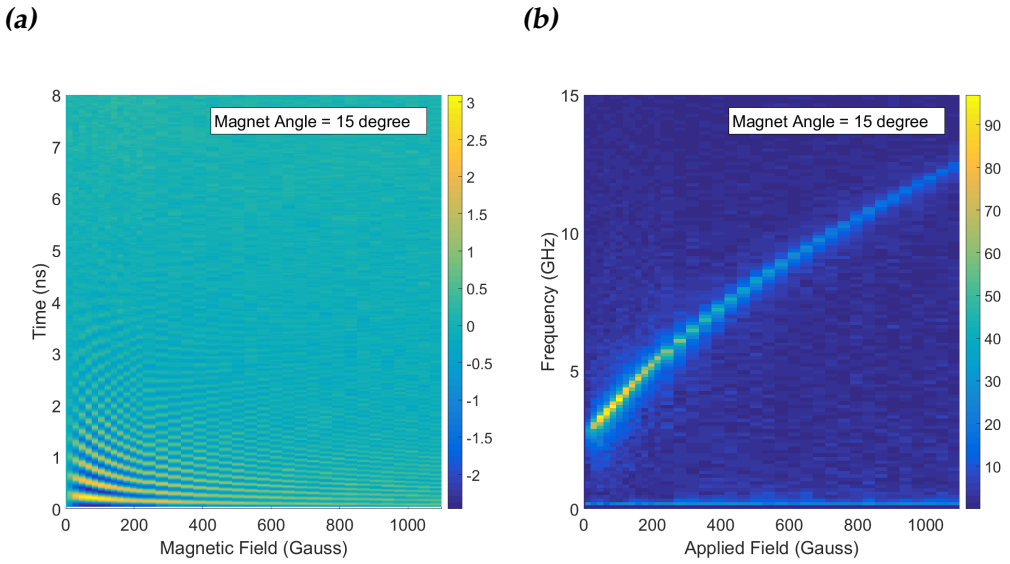

Figure 4.5: *Response of CoFeB/MgO for different applied field strengths. (a) Time traces for different field strengths. (b) Fourier transform of the time traces.*

The offset of the frequency at zero field can be explained by the uniaxial anisotropy, which adds a term to the Kittel equation [17]. The origin of the anisotropy of CoFeB/MgO remains unclear since the method used to produce the sample should result in an amorphous structure. Since this discovery was unexpected and the results not within the scope of the experiment, no research was performed to investigate the origin since it was not in the scope of this research, but there two plausible explanations.

The first explanation is the growth on MgO, which has a (001) orientation. The deposition on this structured substrate can initiate a strain induced magnetic anisotropy. If not initiated at the deposition, pumping the sample the temperature increases by about 300°C, coming close to the crystallization temperature for CoFeB/Mgo [42]. The MgO on which the

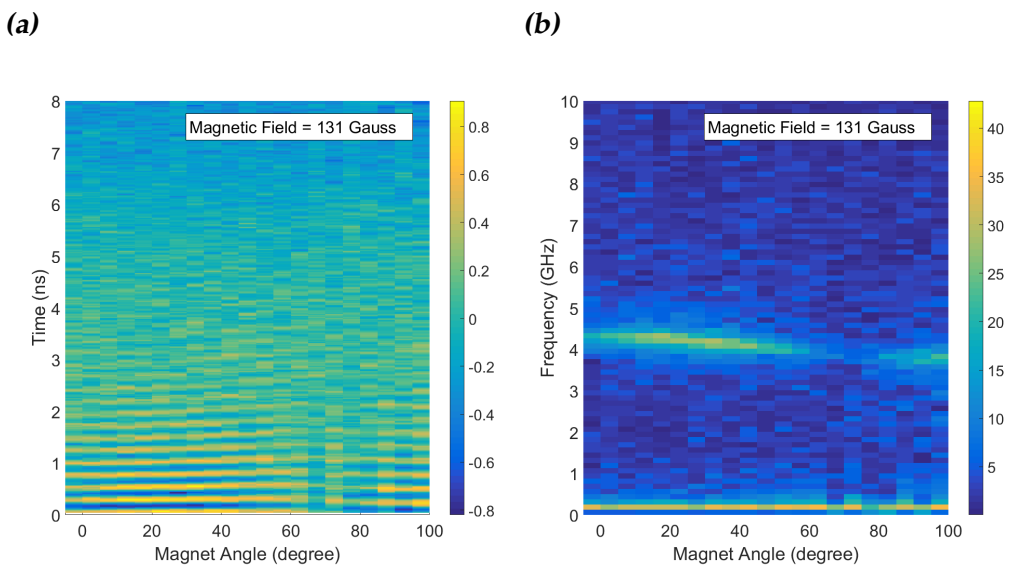

Figure 4.6: *Angular dependence (a) time trace and (b) Fourier transformresonance frequency for CoFeB/SiO$_x$ for the single pump-probe experiment.*

CoFeB is sputtered might act as a template, creating a crystalline interphase between the CoFeB and substrate [43].

The second explanation is the growing of the CoFeB in presence of a small magnetic field. During DC-sputtering, there is a small magnetic field present in the chamber. This magnetic field might have aligned the magnetization of the deposited CoFeB in the uniaxial configuration [20].

The result for CoFeB/SiO$_x$ is given in figure 4.6. From this figure can be concluded that this sample also shows the uniaxial anisotropy with the hard axis around 70°. The easy axis can't be seen in this measurement, but probably will be around $-20°$. However, the signal level of the SiO$_x$ substrate compared to the MgO substrate in figures 4.3 and 4.4a is lower, suggestion a weaker anisotropy constant. This is confimed by the flatter shape which the resonance curve has [17].

Since SiO$_x$ has no structured surface, the annealing of crystalline CoFeB at the MgO interface during pumping the system seems unlikely to be the origin of the anisotropy, suggesting the anisotropy is created during sam-

ple fabrication. This mechanism might be aided by the ordering of the CoFeB on top of the MgO (001), increasing the anisotropic effect for this substrate. However, no evidence has been found for this effect.

4.2 Transient Grating

When introducing the second pump, the interference pattern will cause expansion at the hot regions and contraction at the cold regions. This enables the acoustic waves discussed in section 2.1 to be generated. These acoustic wave may, via inverse magnetostriction, generate the spin precession in the magnetization which are observed via the Faraday detection scheme. Because CoFeB/MgO shows a strong magnetic anisotropic behaviour, the CoFeB/SiO_x sample is chosen to reduce the influence of the anisotropy. Finally, the results of Ni will be discussed and compared to the CoFeB measurements.

4.2.1 Acoustics on CoFeB

The first time trace is shown in figure 4.7 and shows the response for CoFeB/SiO_x for changing applied field strength. In this figure, two main resonance fields can be determined. These field are around $50Gs$ and $205Gs$. These are the fields corresponding to the resonance condition of the SAW and the SSLW respectively. Note that these resonances have the particular phase change at the main resonance field which comes from the phase change of the driven oscillator over the resonance field. This can be seen from the fact that the left side of the resonance has opposite sign from the right side. This follows from the position of the spin relative to the strain field, which changes sign when crossing the resonance field. This can be seen as pushing or pulling of the strain field on the magnetic dipole.

As seen in this figure, the precession for the SAW wave persists for a

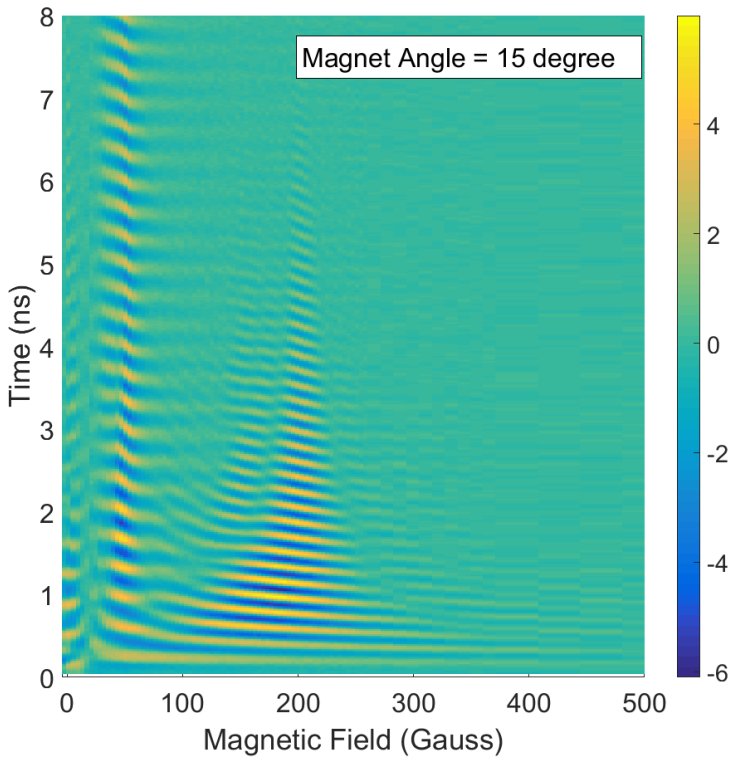

Figure 4.7: *Time trace for the double pump experiment on CoFeB/SiO$_x$.*

longer time than the measured timeframe while the signal coming from the SSLW resonance is gone after $8ns$. This shows that, as expected, the SSLW is damped more strongly. This is explained by the bulk wave behaviour the SSLW possess which dissipates its energy much easier compared to the surface bound SAW wave.

The Fourier transform of this given in figure 4.8. The FMR condition is indicated by the white line. When the FMR condition matches the frequency of the acoustic waves, an increase of signal level is obtained. This increased signal originates from the driven precession caused by the acoustic waves via inverse magnetostriction.

The frequencies found for the acoustic waves are given by the substrate because the grating period lies within the large wavelength limit ($\Lambda > 1\mu m$). The measured frequency for the SiO$_x$ substrate are at $3.0 \pm$

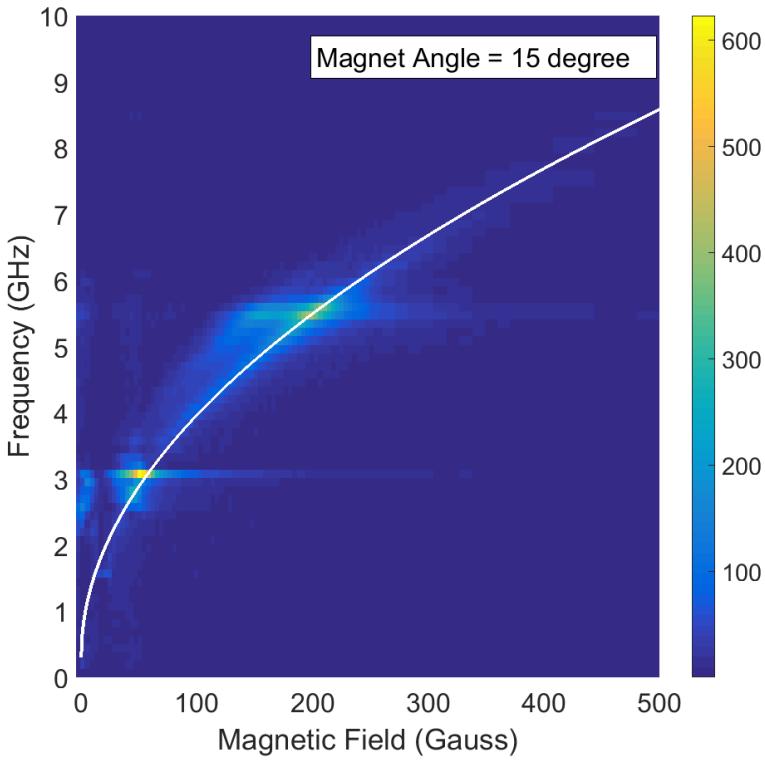

Figure 4.8: *Fourier transform for CoFeB/SiO$_x$. White line is fitted by the Kittel equation with an enabled frequency offset which might be induced by anisotropy. The offset given at zero field is* $0.3GHz$.

$0.1GHz$ for the SAW and $5.4 \pm 0.1GHz$ for the SSLW when a grating of $1.1\mu m$ is applied. These frequencies result in velocities of $3300 \pm 110^{m}/_{s}$ and $6050 \pm 0.1^{m}/_{s}$ respectively. Boechler *et al.* [44] have given the velocities of $3409^{m}/_{s}$ for SAW and $5968^{m}/_{s}$ for SSLW, which lie within the read off error. The velocity might be influenced by the sample deposited on top, which might be the reason for the slightly different velocities [45].

4.2.2 Acoustics on Ni

The second sample which is used is Ni/SLG. The time trace and fourier transform are given in figure 4.9. From this figure, the resonance field for

the SAW and SSLW can be determined, which are 200 and 560Gs respectively. This resonance field lies much higher compared to the 50 and 200Gs for CoFeB obtained from figures 4.7 and 4.8. This is due to the lower saturation magnetization Ni. Equation 2.6 shows the dependence of the FMR frequency and the saturation magnetization. Therefore, the FMR line of Ni has a smaller slope compared to the FMR line of CoFeB/SiO_x which increases the resonance field values for same acoustic velocities.

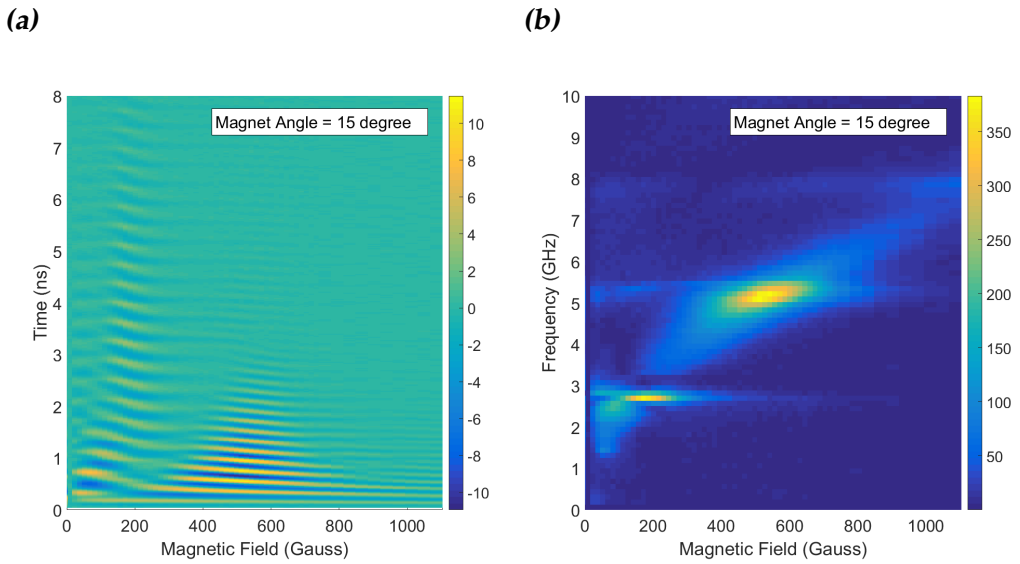

Figure 4.9: *Field dependent scan of Ni/SLG for the double pump experiment. (a) Time trace and (b) its Fourier transform.*

Another important feature is the width of the magnetoelastic resonance. This width is much larger for the Ni sample because of the width of the FMR. This width depends on the Gilbert damping constant according to equation 2.7. The width, depending on the frequency, is expected to increase faster since the damping constant is 10 times as large for Ni compared to CoFeB.

Together with the width of the resonance, so is the duration of the precession given in figure 4.9a dependent on the damping constant. The pre-

cession of the SAW in the Ni has almost died out after $8ns$ while it is still strongly precessing for the CoFeB sample as discussed in the previous section. Also, the precession due to the SSLW persists for only $3ns$ while the precession in CoFeB has died out just before the end of the measurement at $8ns$.

The frequency at which the acoustic waves in the SLG resonate with the larmor precession are $2.9 \pm 0.1GHz$ and $5.3 \pm 0.2GHz$ for SAW and SSLW respectively which are lower compared to the values for the SiO_x sample. These frequencies give $3190 \pm 110^{m}/_{s}$ and $5830 \pm 220^{m}/_{s}$. These velocities match the expected velocities stated in section 2.1.

4.3 Spin Wave Localization

So far, the measurements are done with an applied field angle of 15°. In this section the angle dependent FMR conditions of the CoFeB and Ni samples will be discussed. The measured data will be shown together with the results from the numerical Plane Wave Method (PWM). The latter will be used to predict and explain the results obtained during this research.

4.3.1 CoFeB

Since the resonance field for the SSLW and the SAW frequency change for different applied angles it is not possible to look at only one field strength to obtain information on the angle dependent FMR signal. By taking the integral around the SSLW frequency, $5.4 \pm 0.5GHz$ for CoFeB, the movement of the resonant field strength can be observed and is shown in figure 4.10. Two resonance modes can be found in this figure, one going to lower fields for higher angles and a weak resonance mode is moving to higher fields. The occurrence of multiple resonances is not uncommon and can be interpreted as two different spin wave modes with different energy [27, 46].

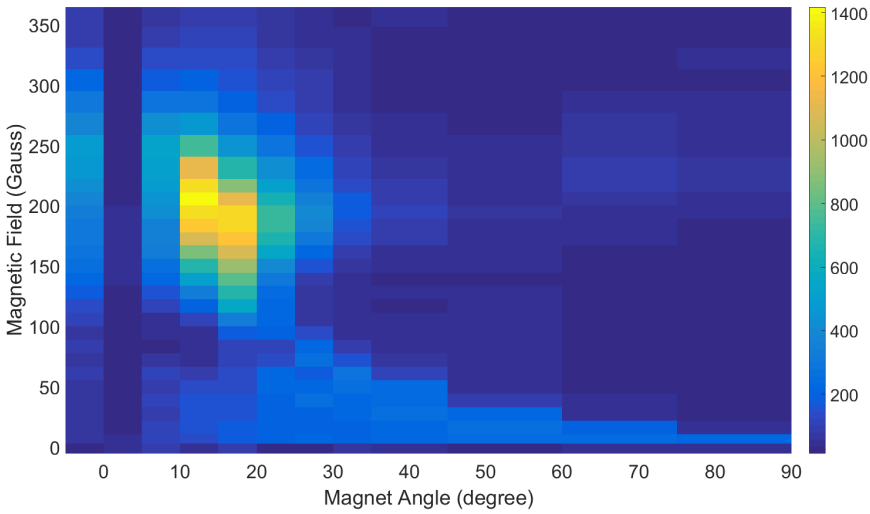

Figure 4.10: *Integrated FFT signal between* 4.9 *and* 5.9GHz *for different applied field angles and applied field angles.*

When integrating over the signal over all applied magnetic field strengths, figure 4.11 is obtained. In this figure, the $\sin(2\phi)$ behaviour which is expected from equation 2.10 is fitted. The theoretical fit, also shown in this figure, is done by external collaborators from the Adam Mickiewicz University in Poznań by using the Plane Wave Method (PWM). Therefore this method won't be discussed, but in short: the method solves the Maxwell's equations by formulating an eigenvalue problem. It is useful to calculate the solutions for the Maxwell's equations over a inhomogeneous or periodic structure in the time-harmonic regime.

For the plane wave method, the assumption was made that the grating period is 1.0μm which is slightly smaller compared the the used grating. The next assumption is that there is a static sinusoidal temperature profile which induces a M/M_s of 0.3 at the heated location and $1M/M_s$ at the cold region. This theoretical fit shows a secondary peak missing in the measurement.

To understand the reason behind the shape of this theoretical signal it is necessary to look at the spin localization for different applied magnetic

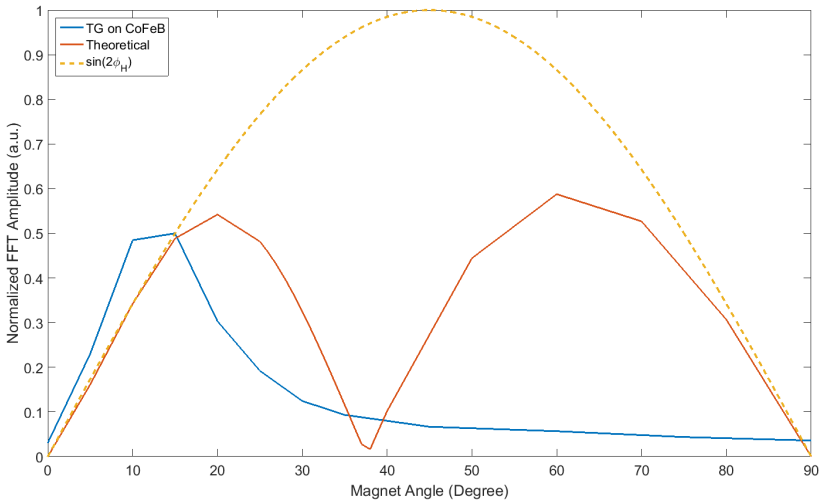

Figure 4.11: *Integrated and normalized fourier transformed signal of the CoFeB/SiO$_x$ angle dependent measurement together with the results of the PWM.*

angles. Since the sample is periodically heated up, the sample will become an MC. The spin wave properties vary in the x-direction of the sample because it has a periodic modulated magnetic landscape.

Figure 4.12 shows this spin localization from the PWM, where $|m|$ is the signal coming from a particular part of the sample. The hot regions expand while the cold regions are being compressed. Therefore the strain ϵ_{xx} of equation 2.11 has opposite sign in either of these regions. The phase is schematically indicated by the arrows in the figure. Because of this opposite strain, the spins are driven out-of-phase in these regions, thereby partially cancelling the signal.

For $\phi = 0°$, the spin localization is almost completely in the cold region and near to no magnetic precession is present in the hot region. Therefore the cold region will mainly contribute to the signal. However, since the magnetization is in the same direction as the strain from the acoustics at zero degree, there is no torque applied on the magnetic moment resulting in a zero signal as seen in figure 4.11.

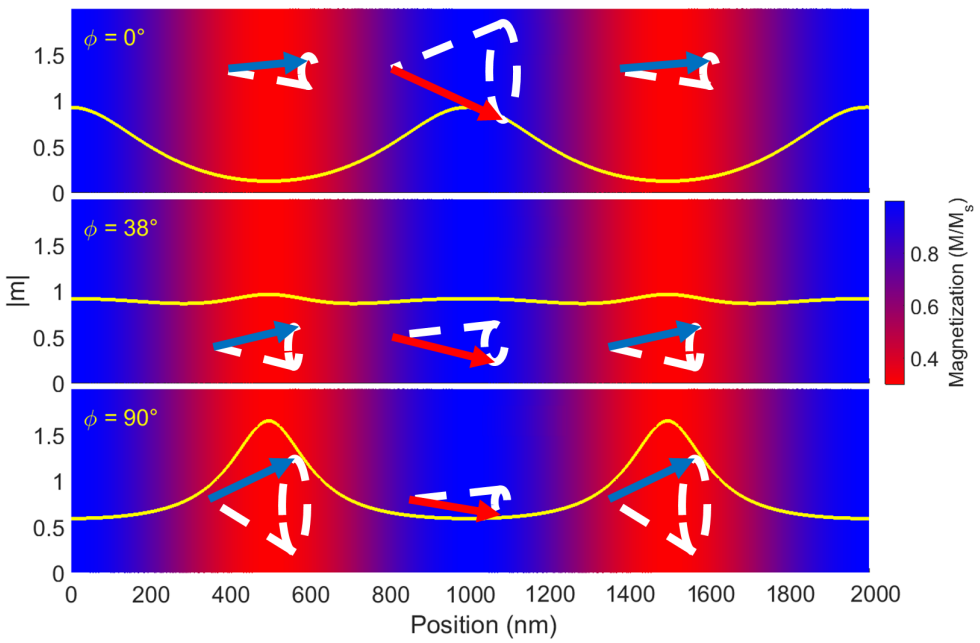

Figure 4.12: *Spin wave localization within the sample at particular angles. Red is heated part because of an interference line and blue is cold part of the sample. The remanent magnetization has a sinusoidal shape.*

When increasing the angle, the $\sin(2\phi)$ increases and therefore the magnetoelastic interaction increases. However, the spins in the hot region of the sample starts to precess with a larger amplitude. Since this precession is out-of-phase compared to the spins in the cold region and the signal obtained by the Faraday detection scheme is the integral over multiple interference lines, the signal disappears at $\phi = 38°$ whereas there is a nonzero value for the magnetoelastic interaction.

With increasing the angle further, the signal from the hot region raises even more and from the cold region decreases, thereby obtaining a difference in signal which can be detected by the Faraday scheme. With increasing the angle, the z-component of the change in magnetization will again decrease and result in zero signal at $\phi = 90°$ even though there is a large spin wave localization at the hot region, just as is the case for 0°. As mentioned earlier, the secondary peak for higher angles is absent for the

measured values. The reason for the absence of the second peak remains unclear and more research is needed to obtain a fundamental explanation. However, suggestions are given in section 4.4, when all results have been discussed.

4.3.2 Ni

Again, the integral over the SSLW frequency can be taken for all different field angles for the Ni/SLG sample. The result of this is shown in figure 4.13. This figure shows two maxima at different angles while the resonance field strength is roughly the same for both maxima. Also in this figure, a weak secondary mode can be seen at the low field value, similar to the one in figure 4.10 for CoFeB.

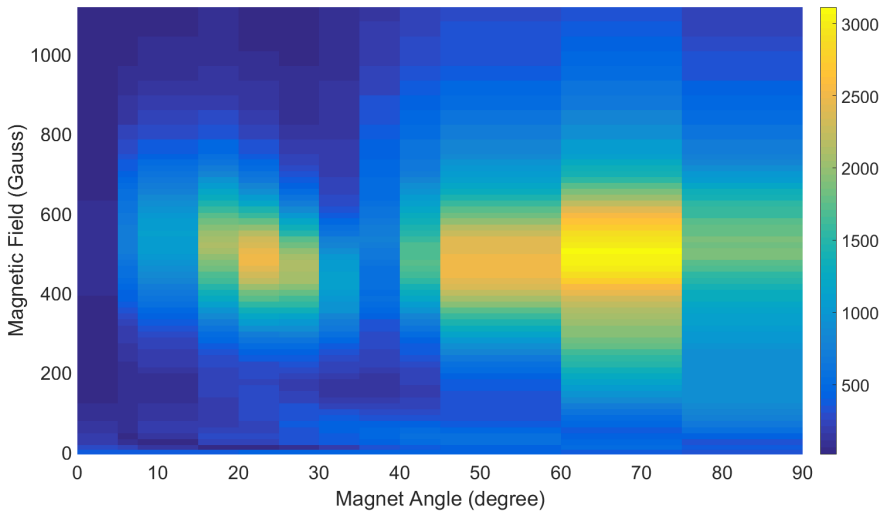

Figure 4.13: *Integrated FFT signal between* $4.4GHz$ *and* $5.5GHz$ *for different applied field angles and applied field angles.*

Figure 4.14 shows the integrated signal over the applied magnetic field strengths. Surprisingly, the second peak which was absent at the CoFeB sample and predicted by the PWM does show up on the Ni sample. Therefore, the spin wave localization seems like a plausible explanation for the

obtained results.

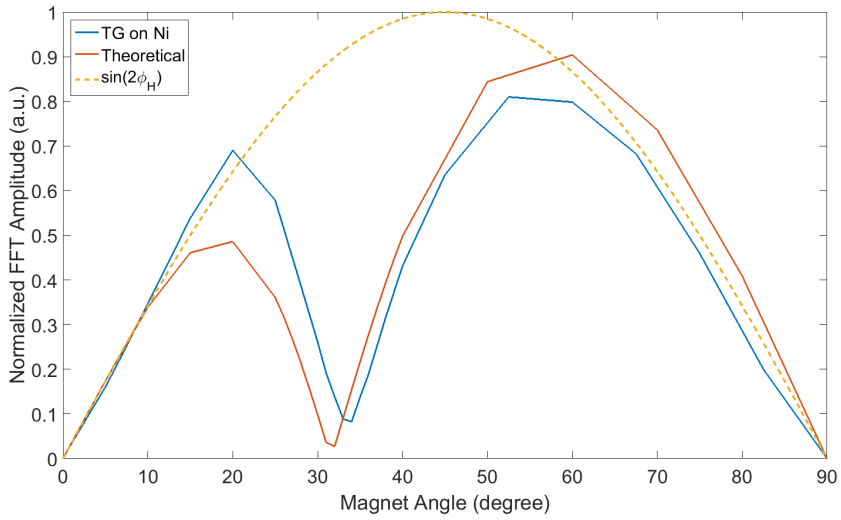

Figure 4.14: *Integrated and normalized signal of the Ni/SLG angle dependent measurement together with the result of the PWM and the* $\sin(2\phi)$ *from the magnetoelastic equation.*

Figure 4.15 shows the spin wave localization on Ni/SLG from the PWM. Again, the assumptions are made that the sample has a periodicity of $1\mu m$ and the magnetization at the hot region is $0.3^{M}/_{M_s}$. Similar result is obtained as for the CoFeB sample, but with a lower angle for the dip at 32° due to the lower saturation magnetization. The spin wave localization for low angles is in the cold region and for high angles it resides mainly in the hot region, which is the same as previously seen for CoFeB.

4.3.3 Ni wires

To verify the obtained results and the suggestion for the spin wave localization theory, Ni wires were produced and measured. These wires have a width of $500nm$ and are spaced $500nm$ apart from each other. The thickness is $50nm$, which is about the same as for the previous Ni and CoFeB samples. Since the wires already have a striped pattern, there is no need

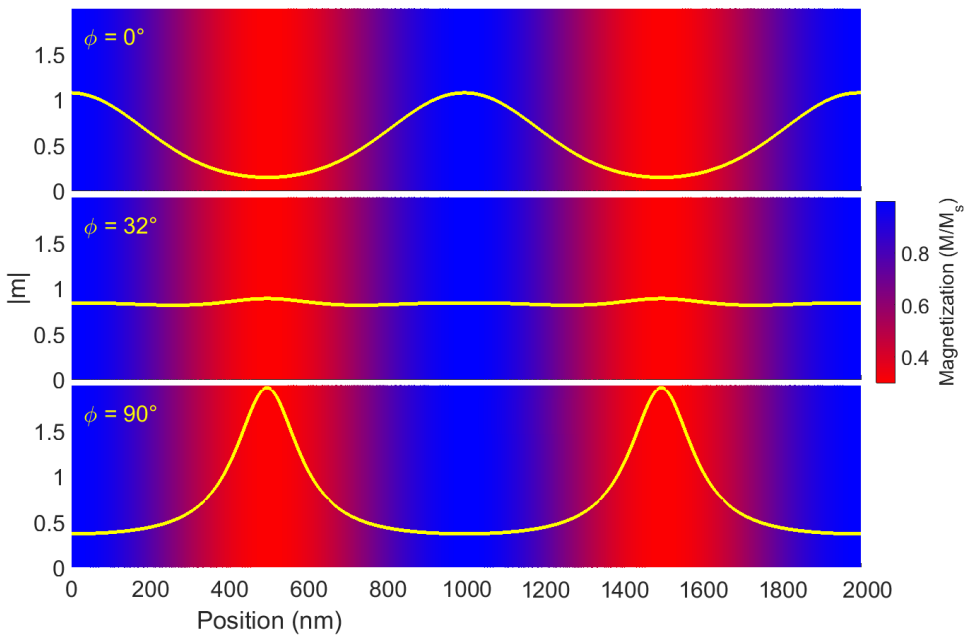

Figure 4.15: *Spin wave localization within the sample at particular angles. Red is heated part because of an interference line and blue is cold part of the sample. The demagnetization has a sinusoidal shape.*

for the second pump; the wired profile is in itself a magnonic crystal since there is no magnetic material in between the stripes. The acoustic waves still propagate since they are transduced by the substrate and not the deposited metal.

The results for the angle dependent measurement is given in figure 4.16. This figure shows again the magnetoelastic interaction curve of $\sin(2\phi)$ and the data from the plain Ni sample with the TG experiment. The last thing it shows is the angle dependence of the Ni wires. From this figure can be seen that the Ni wires follow the magnetoelastic curve. This can be explained by looking at the spin wave localization. Since the cold region in the sample has been removed, the signal comes only from the hot region. Since the signal from the sample is now always in-phase the signal does not get suppressed at a certain angle where the spin is delocalized. The difference in signal on the lower angle side can be explained by the spin

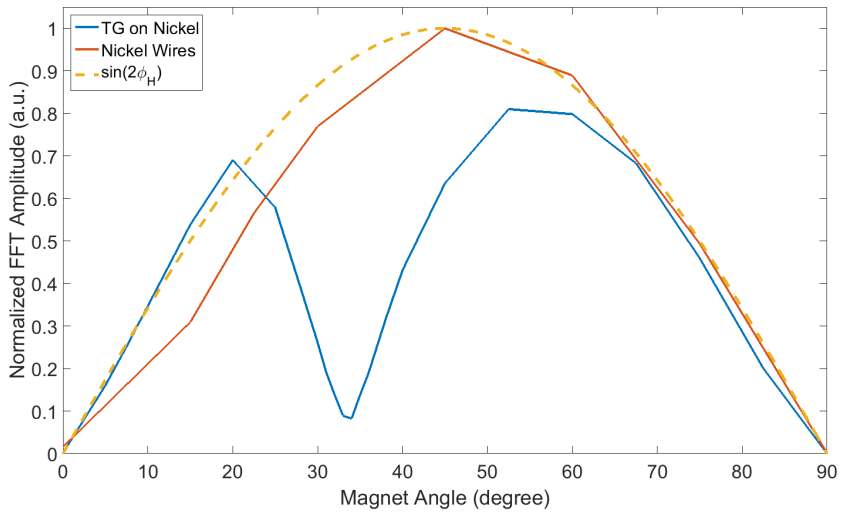

Figure 4.16: *Integrated and normalized signal of the Ni wires on applied magnetic angle dependence together with the obtained signal for TG on nickel and the* $\sin(2\phi)$ *curve from the magnetoelastic interaction.*

wave localization which is still very low at low angles in the hot region as shown in figure 4.15.

4.4 Discussion

Some remarks are necessary on the results obtained in the previous section. The first remark is obviously about the absence of the second peak for the CoFeB sample. Until now, it remains unclear why this peak is missing. Since the setup is the same as for the Ni sample, this feature can't be setup related. Therefore, the differences in properties of CoFeB and Ni should have caused the different properties.

4.4.1 Magnetic Anisotropy

The first difference is the presence of an uniaxial magnetic anisotropy within the CoFeB sample. To find out whether the anisotropic effect in-

terferes with the signal from the acoustics, the sample is rotated on its stage by 25°. This changes the direction of the anisotropic axes. The result of the integrated Fourier transform for the different applied magnetic field angles is shown in figure 4.17.

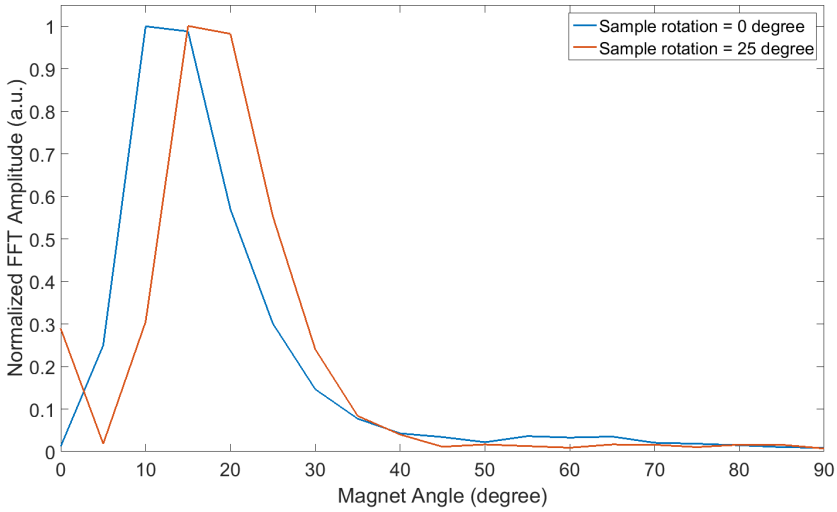

Figure 4.17: *Integrated and normalized signal of the CoFeB/SiO$_x$ angle dependent measurement for two different sample rotation angles.*

This figure shows that the zero value changes by 5° for a sample rotation of 25°. For a sample without anisotropy, this angle should always be at 0° since there is no change of magnetization in the z-axis at this angle as discussed in section 2.5. Because of the anisotropy, the magnetization direction is not the same as the applied field direction, causing the measured shift for different sample orientation.

The shape of both figures stay roughly the same and is only shifted by 5°. From this can be concluded that the anisotropy does not suppress the signal generated by the acoustics within the sample. However, the magnetization direction is slightly influenced when rotating the anisotropy axis and thereby moving the signal to a higher angle.

4.4.2 Spin Wave Localization

For the comparison of the spin wave localization with the results of the PWM, certain assumptions have been made. The periodicity of $1\mu m$ slightly mismatches the grating of $1.1\mu m$ used during the experiment.

Another important assumption is the demagnetization strength. As for the Ni and CoFeB, a demagnetization of $0.3^{M}/_{M_s}$ has been assumed. Since the saturation magnetization of CoFeB is much higher a lower demagnetization effect is expected at the hot region. Also for Ni, the assumption of the depth of the profile isn't correct. By using the model from Janušonis [7] a more accurate temperature profile, and thereby demagnetization profile can be determined.

The demagnetization profile obtained from this model is time-dependent and also includes the thermal redistribution, going to an equally elevated temperature over the whole sample. After $0.5ns$, the minimum magnetization is $0.79^{M}/_{M_s}$ and the maximum at the cold region is $0.95^{M}/_{M_s}$. When using these values, the dip is expected at 40° as shown in figure 4.18, which is higher compared to the measured 32°.

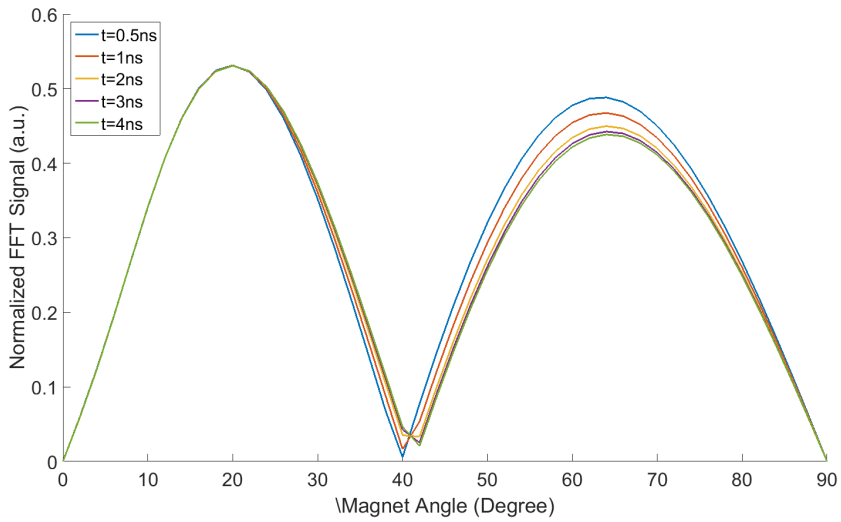

Figure 4.18: *Integrated and normalized FFT signal of the Ni/SLG sample according to the plane wave method. The plot shows the time-dependence of the signal.*

After about $4ns$, the system is almost equally thermally elevated and for both the hot and cold regions the magnetization goes to $0.91^{M}/_{M_s}$. This leads to a time-dependent spin localization as shown in figure 4.18. The dip in this figure, the angle at which there is no spin localization, has moved to higher angles when time passes by. The measurements however give a motion of the dip to lower angles. The origin for this time-dependent movement in the wrong direction has not yet been identified.

For the larger saturation magnetization of CoFeB, an even flatter magnetization profile is expected. The flatter profile moves the dip to higher angles. However, the missing second peak suggests some other contribution to the signal. An explanation could be that the optically induced anisotropy together with the applied field at higher angles are dominant and causes the magnetization to point towards the y-direction. The high saturation magnetization and crystalline anisotropy competes with the optical anisotropy and external magnetic field for the direction of the magnetization. At higher applied field angles, the latter two might be dominant, changing the magnetization direction. Because of this, no change in magnetization in the z-direction is expected according to equation 2.11.

The PWM assumes the magnetization to be in the same direction as the applied field. This assumption might be true for Ni, with its lower saturation magnetization, but might fail for higher M_s values, since a larger field is required to point the magnetization in the direction of the applied field. Therefore the measurements for Ni might show better agreement with the PWM compared to the CoFeB measurements.

However, at $t > 0$, the temperature profile flattens out and after $t = 4ns$ the profile is expected to be almost flat again. Therefore the applied field direction, together with the crystalline anisotropy, determine the direction of the magnetization again. Since the acoustic waves are still present at this time delay, precession is still expected to be driven after a certain time delay. This signal however, does not show up.

Chapter 5

Conclusion

An all-optical pump-probe spectroscopy setup is used to investigate the magnetic and magnetoelastic response in the ferromagnetic materials CoFeB and Ni in an externally in-plane applied magnetic field. First experiments were performed using a single pump to identify the magnetocrystalline anisotropy in the CoFeB for both the MgO and the SiO_x substrate. Uniaxial crystalline anisotropy has been found for both the substrates because of the presence of a hard and an easy axis, which are both in-plane and are perpendicular to each other. The origin of the anisotropy remains unknown, however it is more prominent in the CoFeB/MgO sample. This suggests the anisotropy is induced by a small magnetic field present during fabrication, which may be enhanced by the template structure of the MgO (001).

The second part of this research entails a second pump, simultaneously with the first pump, creating an interference pattern on the sample surface. This interference pattern induces hot stripes on the sample surface, expanding the sample whilst compressing the cold regions. This generated two types of acoustic waves, the Rayleigh surface acoustic wave and the surface skimming longitudinal wave. Measurements are taken on both CoFeB and Ni samples and an enhanced precession is observed at the frequency crossing of the Larmor precession and the acoustic waves. From

this can be concluded that the acoustic waves, induced by the optical transient grating technique, are able to drive the spin precession via inverse magnetostriction at resonance condition.

The last part is about the applied magnetic field angle dependence by using the double pump setup. For the Ni sample, the theory on spin wave localization by using the Plane Wave Method shows promising comparisons with the obtained data. However, when adjusting the parameters for the Plane Wave Method to represent the situation more accurately, the result starts to deviate from the measured values. So does the angle at which the spin delocalize increase to higher angle for less demagnetization. The other discrepancy is the increased delocalization angle over time according to the numerical solution whilst empirically it decreases over time.

For CoFeB, there is a signal at lower angles until 40°. The signal is expected to return according to the Plane Wave Method for higher angles, however, it does not for the measured values. The origin of this absence remains unknown and more research needs to be done to find an explanation for this phenomenon. To eliminate the effect of the crystalline magnetic anisotropy, other measurements should be taken on samples which have larger or smaller anisotropy constants. Another interesting measurement could be on samples with other type of anisotropy, such as cubic anisotropy. To test the effect of the high saturation magnetization, new samples should be taken with different saturation magnetizations to see if the absence of the peak is due to the high saturation magnetization.

Bibliography

[1] P. Elliott, T. Müller, J. K. Dewhurst, S. Sharma, and E. K. U. Gross, *Ultrafast laser induced local magnetization dynamics in Heusler compounds*, Sci. Rep. **6**, 38911 (2016).

[2] F. Ummelen, H. Swagten, and B. Koopmans, *Racetrack memory based on in- plane-field controlled domain-wall pinning*, Sci. Rep. , 1 (2017).

[3] S. Ikeda, J. Hayakawa, Y. Ashizawa, Y. M. Lee, K. Miura, H. Hasegawa, M. Tsunoda, F. Matsukura, and H. Ohno, *Tunnel magnetoresistance of 604% at 300 K by suppression of Ta diffusion in CoFeBMgOCoFeB pseudo-spin-valves annealed at high temperature*, Appl. Phys. Lett. **93**, 1 (2008).

[4] K. Ando, S. Fujita, J. Ito, S. Yuasa, Y. Suzuki, Y. Nakatani, T. Miyazaki, and H. Yoda, *Spin-transfer torque magnetoresistive random-access memory technologies for normally off computing (invited)*, J. Appl. Phys. **115** (2014).

[5] T. Jia, H. Kimura, Z. Cheng, and H. Zhao, *Switching of both local ferroelectric and magnetic domains in multiferroic Bi0.9La0.1FeO3 thin film by mechanical force*, Sci. Rep. **6**, 31867 (2016).

[6] J. Janušonis, C. L. Chang, T. Jansma, A. Gatilova, V. S. Vlasov, A. M. Lomonosov, V. V. Temnov, and R. I. Tobey, *Ultrafast magnetoelastic probing of surface acoustic transients*, Phys. Rev. B - Condens. Matter Mater. Phys. **94**, 1 (2016).

[7] J. Janušonis, T. Jansma, C. L. Chang, Q. Liu, A. Gatilova, A. M. Lomonosov, V. Shalagatskyi, T. Pezeril, V. V. Temnov, and R. I. Tobey, *Transient Grating Spectroscopy in Magnetic Thin Films: Simultaneous Detection of Elastic and Magnetic Dynamics*, Nat. Publ. Gr. , 1 (2016).

[8] M. Zhu, H. Chong, Q. B. Vu, R. Brooks, H. Stamper, and S. Bennett, *Study of CoFeB thickness and composition dependence in a modified CoFeB/MgO/CoFeB perpendicular magnetic tunnel junction*, J. Appl. Phys. **119** (2016).

[9] L. D. Landau and E. M. Lifshitz, *Course of Theoretical Physics, vol. 7, Theory of Elasticity, Landau and Lifshitz*, 1986.

[10] C. Campbell, *Surface Acoustic Wave Devices and Their Signal Processing Applications*, Academic Press, Inc, 1989.

[11] R. Lacombe, *Adhesion Measurement Methods: Theory and Practice*, Taylor & Francis Group, 1996.

[12] A. Habib, A. Shelke, M. Pluta, U. Pietsch, T. Kundu, and W. Grill, *Scattering and attenuation of surface acoustic waves and surface skimming longitudinal polarized bulk waves imaged by Coulomb coupling*, **247**, 247 (2012).

[13] C. Kittel, *Introduction to solid state physics*, volume Third, John Wiley & Sons, Inc, Hoboken, 8th editio edition, 1953.

[14] S. Blundell, *Magnetism in Condensed Matter*, volume 1, Oxford University Press, Oxford, first edition, 2001.

[15] Griffiths J. H. E., *Anomalous High-frequency Resistance of Ferromagnetic Metals*, Nature **158**, 670 (1946).

[16] C. Kittel, *On the theory of ferromagnetic resonance absorption*, Phys. Rev. **73**, 155 (1948).

[17] M. Farle, *Ferromagnetic resonance of ultrathin metallic layers*, Rep. Prog. Phys. **61**, 755 (1998).

[18] J. M. Beaujour, D. Ravelosona, I. Tudosa, E. E. Fullerton, and A. D. Kent, *Ferromagnetic resonance linewidth in ultrathin films with perpendicular magnetic anisotropy*, Phys. Rev. B - Condens. Matter Mater. Phys. **80**, 2 (2009).

[19] A. J. Berger, W. Amamou, S. P. White, R. Adur, Y. Pu, R. K. Kawakami, and P. C. Hammel, *Magnetization dynamics of cobalt grown on graphene*, J. Appl. Phys. **115**, 1 (2014).

[20] D. Kirk, A. Kohn, K. B. Borisenko, C. Lang, J. Schmalhorst, G. Reiss, and D. J. H. Cockayne, *Structural study of amorphous CoFeB thin films exhibiting in-plane uniaxial magnetic anisotropy*, Phys. Rev. B - Condens. Matter Mater. Phys. **79**, 1 (2009).

[21] X. Qiao, B. Wang, Z. Tang, Y. Shen, H. Yang, J. Wang, Q. Zhan, S. Mao, X. Xu, and R. W. Li, *Tuning magnetic anisotropy of amorphous CoFeB film by depositing on convex flexible substrates*, AIP Adv. **6** (2016).

[22] S. A. Manuilov, A. M. Grishin, and M. Munakata, *Ferromagnetic resonance, magnetic susceptibility, and transformation of domain structure in CoFeB film with growth induced anisotropy*, J. Appl. Phys. **109** (2011).

[23] M. Yamanouchi, A. Jander, P. Dhagat, S. Ikeda, F. Matsukura, and H. Ohno, *Domain Structure in CoFeB Thin Films With Perpendicular Magnetic Anisotropy*, IEEE Magn. Lett. **2**, 3000304 (2011).

[24] S. Ikeda, K. Miura, H. Yamamoto, K. Mizunuma, H. D. Gan, M. Endo, S. Kanai, J. Hayakawa, F. Matsukura, and H. Ohno, *A perpendicular-anisotropy CoFeB–MgO magnetic tunnel junction*, Nat. Mater. **9**, 721 (2010).

[25] H. Sato, M. Yamanouchi, S. Ikeda, S. Fukami, F. Matsukura, and H. Ohno, *Perpendicular-anisotropy CoFeB-MgO magnetic tunnel junctions with a MgO/CoFeB/Ta/CoFeB/MgO recording structure*, Appl. Phys. Lett. **101** (2012).

[26] O. Kovalenko, T. Pezeril, and V. V. Temnov, *New concept for magnetization switching by ultrafast acoustic pulses*, Phys. Rev. Lett. **110**, 1 (2013).

[27] M. Langer, F. Röder, R. A. Gallardo, T. Schneider, S. Stienen, C. Gatel, R. Hübner, A. Roldán-Molina, L. Bischoff, K. Lenz, J. Lindner, P. Landeros, and J. Fassbender, *The role of the internal demagnetizing field in a surface-modulated magnonic crystal*, arXiv , 1 (2016).

[28] M. Krawczyk and D. Grundler, *Review and prospects of magnonic crystals and devices with reprogrammable band structure.*, J. Phys. Condens. Matter **26**, 123202 (2014).

[29] M. Faraday, *On the magnetization of light and the illumination of magnetic lines of force*, Philos. Trans. R. Soc. London **136**, 1 (1846).

[30] E. Hecht, *Optics*, Pearson Education, San Francisco, fourth edition, 2002.

[31] A. Jain, *A simple experiment for determining Verdet constants using alternating current magnetic fields*, Am. J. Phys. **67**, 714 (1999).

[32] X. Liu, W. Zhang, M. J. Carter, and G. Xiao, *Ferromagnetic resonance and damping properties of CoFeB thin films as free layers in MgO-based magnetic tunnel junctions*, J. Appl. Phys. **110** (2011).

[33] S. Iihama, S. Mizukami, H. Naganuma, M. Oogane, Y. Ando, and T. Miyazaki, *Gilbert damping constants of Ta/CoFeB/MgO(Ta) thin films measured by optical detection of precessional magnetization dynamics*, Phys. Rev. B - Condens. Matter Mater. Phys. **89**, 1 (2014).

[34] A. Natarajarathinam, Z. R. Tadisina, T. Mewes, S. Watts, E. Chen, and S. Gupta, *Influence of capping layers on CoFeB anisotropy and damping*, J. Appl. Phys. **112**, 1 (2012).

[35] J. Walowski, M. Djordjevic, B. Lenk, C. Hamann, J. McCord, and M. Münzenberg, *Intrinsic and non-local Gilbert damping in polycrystalline nickel studied by Ti:sapphire laser fs spectroscopy*, J. Phys. D. Appl. Phys. **41**, 164016 (2008).

[36] T. Satoh, Y. Terui, R. Moriya, B. a. Ivanov, K. Ando, E. Saitoh, T. Shimura, and K. Kuroda, *Directional control of spin-wave emission by spatially shaped light*, Nat. Photonics **6**, 662 (2012).

[37] Y. Liu, L. Shelford, V. Kruglyak, R. Hicken, Y. Sakuraba, M. Oogane, Y. Ando, and T. Miyazaki, *Ultrafast Optical Modification of Magnetic Anisotropy and Stimulated Precession in an Epitaxial Co2MnAl Thin Film*, J. Appl. Phys. **101** (2007).

[38] B. Koopmans, M. Van Kampen, J. T. Kohlhepp, and W. J. M. De Jonge, *Ultrafast magneto-optics in nickel: magnetism or optics?*, Phys. Rev. Lett. **85**, 844 (2000).

[39] M. van Kampen, C. Jozsa, J. T. Kohlhepp, P. LeClair, L. Lagae, W. J. M. de Jonge, and B. Koopmans, *All-optical probe of coherent spin waves*, Phys. Rev. Lett. **88**, 227201/1 (2002).

[40] J. A. Rogers, A. A. Maznev, M. J. Banet, and K. A. Nelson, *Optical Generation and Characterization of Acoustic Waves in Thin Films*, Annu. Rev. Mater. Sci. **30**, 117 (2000).

[41] V. Gusev, *On generation of picosecond inhomogeneous shear strain fronts by laser-induced gratings*, Appl. Phys. Lett. **94** (2009).

[42] T. Ibusuki, T. Miyajima, S. Umehara, S. Eguchi, and M. Sato, *Lower-temperature crystallization of CoFeB in MgO magnetic tunnel junctions by using Ti capping layer*, Appl. Phys. Lett. **94**, 1 (2009).

[43] S. Yuasa, Y. Suzuki, T. Katayama, and K. Ando, *Characterization of growth and crystallization processes in CoFeBMgOCoFeB magnetic tunnel junction structure by reflective high-energy electron diffraction*, Appl. Phys. Lett. **87**, 1 (2005).

[44] N. Boechler, J. K. Eliason, A. Kumar, A. A. Maznev, K. A. Nelson, and N. Fang, *Interaction of a contact resonance of microspheres with surface acoustic waves*, Phys. Rev. Lett. **111** (2013).

[45] I. Touati, Z. Hadjoub, L. Touati-Tilba, and A. Doghmane, *Influence of Elastic Properties of Thin Films deposited on Si and/or Mg substrates on Rayleigh velocity dispersion evolution*, Phys. Procedia **2**, 899 (2009).

[46] C. Schoeppner, K. Wagner, S. Stienen, R. Meckenstock, M. Farle, R. Narkowicz, D. Suter, and J. Lindner, *Angular dependent ferromagnetic resonance analysis in a single micron sized cobalt stripe*, J. Appl. Phys. **116**, 1 (2014).